ORIGINAL PAPER

An extended biphasic model for charged hydrated tissues with application to the intervertebral disc

W. Ehlers · N. Karajan · B. Markert

Abstract Finite element models for hydrated soft biological tissue are numerous but often exhibit certain essential deficiencies concerning the reproduction of relevant mechanical and electro-chemical responses. As a matter of fact, single-phasic models can never predict the interstitial fluid flow or related effects like osmosis. Quite a few models have more than one constituent, but are often restricted to the small-strain domain, are not capable of capturing the intrinsic viscoelasticity of the solid skeleton, or do not account for a collagen fibre reinforcement. It is the goal of this contribution to overcome these drawbacks and to present a thermodynamically consistent model, which is formulated in a very general way in order to reproduce the behaviour of almost any charged hydrated tissue. Herein, the Theory of Porous Media (TPM) is applied in combination with polyconvex *Ogden*-type material laws describing the anisotropic and intrinsically viscoelastic behaviour of the solid matrix on the basis of a generalised *Maxwell* model. Moreover, other features like the deformation-dependent permeability, the possibility to include inhomogeneities like varying fibre alignment and behaviour, or osmotic effects based on the simplifying assumption of *Lanir* are also included. Finally, the human intervertebral disc is chosen as a representative for complex soft biological tissue behaviour. In this regard, two numerical examples will be presented with focus on the viscoelastic and osmotic capacity of the model.

W. Ehlers (✉) · N. Karajan · B. Markert
Institute of Applied Mechanics (Civil Engineering),
University of Stuttgart, Pfaffenwaldring 7,
70569 Stuttgart, Germany
e-mail: ehlers@mechbau.uni-stuttgart.de
URL: http://www.mechbau.uni-stuttgart.de/ls2

N. Karajan
e-mail: karajan@mechbau.uni-stuttgart.de

B. Markert
e-mail: markert@mechbau.uni-stuttgart.de

1 Introduction and overview

Finite element models of hydrated soft biological tissues can remarkably aid the design of new implants, thereby serving as a diagnostic tool or numerical laboratory. In the context of spine mechanics, the intervertebral disc (IVD) plays a key role, as it is a representative for complex soft biological tissue behaviour dominating the overall mechanical performance of the spine. Hence, the IVD is chosen for the development of a general model describing several relevant effects.

Note in passing that in industrialised western countries, almost everybody has been suffering from low back pain (LBP) at least once in his lifetime, e. g., in a representative survey carried out in the early nineties and another one conducted ten years later, about 85 % of the German population had already experienced this widespread ailment. cf. Raspe et al. 2008; Schmidt et al. 2007. Moreover, LBP is the number one cause of work related health problems in many European countries. The fourth European survey on working conditions in 2007 reported an overall average of 25% of the working people in Europe suffering from LBP (Parent-Thirion et al. 2007). This clearly reveals the need for research in the field of IVD mechanics, in order to better understand the complex, coupled behaviour of the IVD and its influence on the overall performance.

Before discussing the features of an appropriate finite element model, a short overview of the necessary tissue properties is given. For a more detailed description, the reader is referred to Urban and Roberts (1996), Ayad and Weiss (1987), Mow and Hayes (1997), Marchand and Ahmed (1990), Ehlers et al. (2006b) and references therein. As the name implies, the IVD is embedded in between two vertebrae, where the cartilaginous endplates build the transition between the disc and the bony vertebrae but will not be addressed separately in this contribution. Two main regions can be distinguished in an axial cut through the IVD, a gelatinous core, the nucleus pulposus (NP) enclosed by a fibrous, lamellar structure, the anulus fibrosus (AF). Both regions are composed of a porous multi-component microstructure consisting of a charged, hydrated extracellular matrix (ECM) as well as an ionised interstitial fluid yielding a swelling-active material. The ECM, also referred to as solid skeleton, consists of proteoglycans (PGs), glycosaminoglycans (GAGs), and collagen fibres of type I and II saturated by a liquid containing dissolved anions and cations as solutes. In this regard, the collagen of type I forms large parallel fibre bundles representing the structural collagen in the AF, whereas the collagen of type II is distributed statistically equal, thereby forming a loose network of fibrils contributing to the isotropic behaviour of the NP. The relatively large PGs and GAGs carry negative fixed charges, but cannot move freely as they are trapped in the fine collagen network. Thus, the fixed negative charges underly the same movement as the whole solid matrix. Apart from that, the fixed charge density (FCD) is highest in the NP and lowest at the perimeter of the AF (Iatridis et al. 2003; Urban and Holm 1986; Urban and Roberts 1996). Moreover, the structural collagen is inhomogeneously distributed throughout the AF concerning its alignment as well as its occurrence yielding varying mechanical properties of the lamellae (Holzapfel et al. 2005; Eberlein et al. 2004; Ebara et al. 1996; Skaggs et al. 1994). Finally, the IVD is characterised by a coupled dissipative behaviour resulting from the viscous fluid flow, the intrinsic viscoelasticity of the ECM protein meshwork and the resulting swelling phenomena (Ehlers and Markert 2001; Ehlers et al. 2002; Iatridis et al. 1996, 1997 and references therein) . Thus, all the properties characterising soft biological tissues in general are unified within the IVD.

Currently, there are several models and modules available, which are used to describe soft biological tissues in general. However, most of them do not cover all the requirements needed for the continuum mechanical modelling of the IVD. For example, the models used for state-of-the-art simulations of the spine are often restricted to singlephasic materials, thereby a priori excluding effects resulting from interstitial fluid flow and osmosis. The first spine simulations with an advanced IVD model were carried out by Shirazi-Adl (1994, 2006) or Shirazi-Adl et al. (1986a,b) using a deformation-dependent *Hooke*-type material tangent and non-linear spring elements to capture the collagen fibres in the AF. In order to overcome the resulting grid dependency of the alignment of the spring elements, the anisotropic continuum theory based on Spencer (1972, 1982) and Boehler (1987) was adopted and applied to the unique behaviour of the collagen fibres by, e. g., Klisch and Lotz (1999), Elliott and Setton (2000) or Holzapfel and Gasser (2001), whereas Schröder and Neff (2003), Balzani et al. (2005) or Markert et al. (2005) further developed the theory towards a polyconvex framework. This knowledge was then incorporated in the lumbar spine simulations of Eberlein et al. (2001, 2004).

Since these models are singlephasic, they do not account for the fluid flow in the disc which is important for nutritional purposes and maintaining the biological composition (Holm and Nachemson 1983; Urban and Holm 1986). Hence, at least a second phase, the interstitial fluid, has to be introduced to overcome this deficiency. In this context, several biphasic models, based on the works of Biot (1941), Bowen (1976) and Mow et al. (1980), are applied to describe soft biological tissues in general or with application to the IVD (Argoubi and Shirazi-Adl 1996; Iatridis et al. 1998; Klisch and Lotz 2000; Ayotte et al. 2000; Li et al. 1999, 2003; Riches et al. 2002). However, as the occurring osmotic effects influence the fluid flow in the tissue, it also has to be considered. In order to include these electro-chemomechanically driven swelling phenomena, the biphasic models need to be extended which can be accomplished in two different approaches. On the one hand, there is an independent description of the freely movable ions of the pore fluid yielding a complex and strongly coupled system of partial differential equations (PDE) leading to a difficult numerical treatment (Frijns et al. 1997, 2003; Ehlers et al. 2002; Huyghe et al. 2003; Kaasschieter et al. 2003; Lai et al. 1991; van Loon et al. 2003; Sun et al. 1999). On the other hand, a much simpler algorithm capable of describing osmosis is based on the assumption of an instantaneous chemical equilibrium throughout the domain of the IVD (Lanir 1987). Following this, only the solid skeleton is extended by the almost volume-free, fixed negative charges and a constitutively computed osmotic pressure is added to the hydrostatic pressure. This procedure is adopted in the context of a two-phase model by Laible et al. (1993), Iatridis et al. (2003), Hsieh et al. (2005) or Ehlers et al. (2006b). A comparison of the two approaches yields a good approximation of the exact solution for the simplified model, even when simulating sudden concentration changes in the external solution (Wilson et al. 2005). However, as sudden changes in the surrounding concentration are usually not applicable for living organisms, *Lanir*'s assumption is perfectly suitable for the numerical simulation of the IVD for instance.

Most of the models in the above cited works suffer from the limitation to the small strain domain with often purely elastic material behaviour. In contrast, the solid skeleton of soft
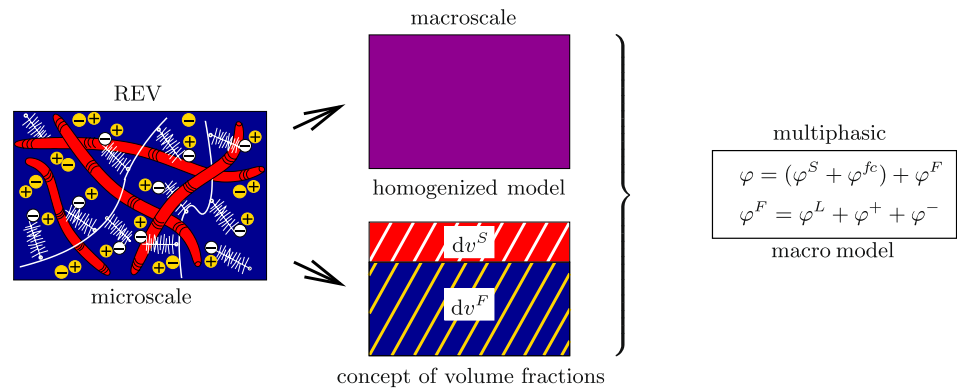
biological tissues or cartilage emerges intrinsic viscoelastic properties, see, e.g., Hayes and Bodine (1978) and Ehlers and Markert (2001) among others. In this regard, it is still not clear, to what extent intrinsic viscoelastic effects stem from the proteoglycans, the loose (type II) collagen network, or the structural (type I) collagen. In this contribution, only the isotropic part of the solid matrix including the randomly distributed type II collagen is modelled to be viscoelastic, while the structural collagen fibres of type I remain hyperelastic. The reason for this assumption becomes clear when the findings of Holzapfel et al. (2005) are observed, stating that there was little to no rate dependency when a lamella of the AF is pulled in fibre direction. Hence, the dissipative effects must stem from the isotropic part of the matrix.

Moreover, the efficient numerical treatment of the governing equations is often not implemented, and therefore, the presented numerical examples are restricted to rather simple 1-d and 2-d boundary-value problems (BVP), respectively. Thus, the goal of this contribution is to present a thermodynamically consistent model based on the well-founded Theory of Porous Media (TPM), cf. Bowen (1980), Mow et al. (1989), de Boer (2000) and Ehlers (2002), which is suitable for the simulation of any electro-chemically active soft biological tissues in general and the IVD in particular. In addition, the respective constitutive equations needed to include the anisotropic and viscoelastic material behaviour as well as the osmotic pressure are presented in a modular manner allowing for a convenient handling. Finally, the efficiency of the model is shown by two fully coupled 3-d simulations. Firstly, a torsional shear experiment is used to fit the viscoelastic parameters to the experimental findings of Iatridis et al. (1997), which are then taken for a swelling experiment of the nucleus pulposus in an ex vivo sagittally cut IVD.

2 Theory of Porous Media (TPM)

The TPM, originally designed for geotechnical problems, is a well-founded macroscopic continuum theory, which is based on the theory of mixtures extended by the concept of volume fractions, (Bowen 1980; Mow et al. 1989; de Boer 2000; Ehlers 2002). In the case of a liquid-saturated linear elastic and quasi-static material behaviour in the small strain domain, the TPM results in the same set of equations as the theory of Biot (1941) (Schanz and Diebels 2003). However, when extended to finite deformations with varying porosity in combination with arbitrary, non-linear dissipative material laws, the TPM offers a transparent theoretical access regarding the separation of the balance and constitutive equations. In contrast to *Biot*'s constitutively derived theory, the TPM approach allows for a clear identification of materially independent equations (i.e., balance equations) and so-called constitutive equations characterising the material behaviour (i.e., viscoelasticity, anisotropy or osmosis), thereby ensuring a convenient modular character of the overall theoretical framework.

Proceeding from a binary aggregate composed of solid and fluid constituents φ^α denoted by $\alpha = \{S, F\}$, the solid phase (i.e., the ECM consisting of PGs, GAGs and collagen) is extended by incorporating the almost volume-free fixed negative charges φ^{fc} (Fig. 1). Furthermore, the interstitial fluid φ^F as an ionic solution is composed of water as a liquid solvent φ^L and mobile electrolytes (Na^+Cl^-) as solutes φ^+ and φ^-. In this context, it is assumed that all constituents φ^α are statistically equal distributed throughout a representative elementary volume (REV). Hence, a real or a virtual averaging process over the REV is possible finally leading to a model of superimposed and interacting continua, i.e., the homogenised or 'smeared' model.

Following this leads to a quadriphasic model describing each of the solutes φ^+ and φ^- independently (Frijns et al. 1997). Exploiting the electroneutrality condition allows for a reduction to a triphasic model yielding a decrease of the primary variables from four to three (i.e., the solid displacement, the hydraulic pressure and the cation concentration) as is described in, e.g., Ehlers et al. (2002, 2005). However, the first benchmark computations on simple geometries using the triphasic displacement-pressure-concentration formulation

were accompanied by oscillations and a general numerical instability (Ehlers and Acartürk 2007). The cause of the oscillations can be traced back to the dependence of the concentration boundary condition (BC) on the solution of the solid displacement field inside the domain. A numerical stabilisation is only possible if the BC is weakly fulfilled and included in the iteration process (Ehlers et al. 2005). Hence, an alternative modelling ansatz must be applied, bearing in mind that future simulations of the intensely inhomogeneous, anisotropic IVD (including the much stiffer, adjacent vertebrae) already evolve several other numerical difficulties. Note in passing, that other triphasic theories which exhibit four primary degrees of freedom, i.e., solid displacement and three modified chemical potentials for water, cations and anions, do not suffer from these oscillations (Lai et al. 1991; Sun et al. 1999).

As already mentioned in the introduction, it is possible to further reduce this model by applying the assumption of Lanir (1987) stating that the tiny mobile ions are assumed to diffuse rapidly through the liquid and by themselves, do not give rise to concentration gradients. In the context of living soft biological tissues, such as the IVD, this simplification makes sense because sudden concentration changes of the surrounding fluid yielding large perturbations of the chemical equilibrium do not occur. Hence, the soft biological tissue is always immediately in electro-chemical equilibrium, which allows the application of the Donnan (1911) equilibrium not only at the domain boundary but also in the inside. The arising osmotic properties can therefore be sufficiently described without considering the ion concentrations (or electro-chemical potentials) as additional unknowns of the process. The resulting osmotic pressure is simply computed via a constitutive equation depending on the fixed charge density inside the domain and added to the hydraulic pore pressure. The result is an extended biphasic formulation consisting of a fully saturated solid skeleton carrying volume-free fixed negative charges and an incompressible pore fluid.

In this context, the volume fractions $n^\alpha = dv^\alpha/dv$ (partial volume dv^α per bulk volume dv) serve as describing physical quantities consistent with the saturation constraint

$$\sum_\alpha n^\alpha = n^S + n^F = 1, \quad \text{where } n^{fc} \approx 0. \tag{1}$$

Exploiting the definition of the volume fractions n^α, a partial density $\rho^\alpha = dm^\alpha/dv$ (constituent mass m^α) and a material or realistic density $\rho^{\alpha R} = dm^\alpha/dv^\alpha$ can be defined for each constituent φ^α, which are related to each other via

$$\rho^\alpha = n^\alpha \rho^{\alpha R}. \tag{2}$$

The kinematics for such an ansatz is based on the framework of superimposed continua, where each spatial point $\mathbf{x}$ of the current configuration is at any time t simultaneously occupied by material points P^α of all constituents. Following this, all particles proceed from different reference positions $\mathbf{X}_\alpha$, which leads to individual motion and velocity fields for each constituent reading

$$\mathbf{x} = \chi_\alpha(\mathbf{X}_\alpha, t) \quad \text{and} \quad \mathbf{x}'_\alpha = \frac{d\chi_\alpha(\mathbf{X}_\alpha, t)}{dt}, \tag{3}$$

respectively. Therein, $(\cdot)'_\alpha$ denotes the material time derivative following the motion of φ^α. Describing multiphasic materials, it is convenient to express the solid in a *Lagrange*an setting via the displacement vector $\mathbf{u}_S = \mathbf{x} - \mathbf{X}_S$ and the overall fluid in a modified *Euler*ian setting relative to the deforming solid skeleton through the seepage velocity $\mathbf{w}_F = \mathbf{x}'_F - \mathbf{x}'_S$. Furthermore, the fixed charges are assumed to move with the deforming solid skeleton described by the solid deformation gradient given by $\mathbf{F}_S = \partial\mathbf{x}/\partial\mathbf{X}_S$.

3 Balance relations

Materially independent balance equations are needed to solve for the previously introduced unknown field quantities, i.e., the solid displacement $\mathbf{u}_S$ and the seepage velocity $\mathbf{w}_F$ as well as to restrict the necessary constitutive equations needed to close the set of equations. In this context, the mass and the momentum balances for each of the constituents are usually applied as well as the entropy inequality. Moreover, the model under consideration is assumed to be composed of materially incompressible constituents (defined by $\rho^{\alpha R} = \text{const.}$), which is always valid for the case of soft biological tissues under physiological levels of pressure (Bachrach et al 1998), yielding a reduction of the mass balance to a volume balance. Note in passing that the property of material incompressibility does not lead to a macroscopic incompressibility as the partial density ρ^α can still change through changes in the volume fraction n^α, cf. Eq. (2). Furthermore, all thermal effects as well as internal mass productions are neglected in this contribution, thereby excluding any biochemical reactions and growth processes. Proceeding from quasi-static and isothermal conditions in accordance to Ehlers (2002), the respective volume and momentum balances as well as the entropy inequality in the *Clausius–Planck* form for the solid and fluid constituents (denoted by α) read

$$(n^\alpha)'_\alpha + n^\alpha \operatorname{div} \mathbf{x}'_\alpha = 0,$$
$$\operatorname{div} \mathbf{T}^\alpha + \rho^\alpha \mathbf{b} + \hat{\mathbf{p}}^\alpha = \mathbf{0}, \tag{4}$$
$$\sum_\alpha (\mathbf{T}^\alpha \cdot \mathbf{L}_\alpha - \rho^\alpha (\psi^\alpha)'_\alpha - \hat{\mathbf{p}}^\alpha \cdot \mathbf{x}'_\alpha) \geq 0.$$

Herein, $\mathbf{T}^\alpha$ is the partial *Cauchy* stress tensor and $\rho^\alpha \mathbf{b}$ is the body force. Furthermore, a measure for the produced interaction force of the fluid while it percolates through the pore space is represented by the direct momentum production

term $\hat{\mathbf{p}}^\alpha$ satisfying the conservation constraint $\hat{\mathbf{p}}^S + \hat{\mathbf{p}}^F = \mathbf{0}$. The spatial velocity gradient is denoted by $\mathbf{L}_\alpha = \mathrm{grad}\, \mathbf{x}'_\alpha$, while ψ^α stands for the *Helmholtz* free energy. As usual for multi-component models, Eqs. (4) are combined for the solid and the fluid phase yielding the respective set of governing equations for the overall aggregate in local form

$$\mathrm{div}\,[(\mathbf{u}_S)'_S + n^F \mathbf{w}_F] = 0,$$

$$\mathrm{div}\,(\mathbf{T}^S + \mathbf{T}^F) + (n^S \rho^{SR} + n^F \rho^{FR})\,\mathbf{b} = \mathbf{0}, \qquad (5)$$

$$\mathbf{T}^S \cdot \mathbf{L}_S - \rho^S (\psi^S)'_S + \mathbf{T}^F \cdot \mathbf{L}_F - \rho^F (\psi^F)'_F - \hat{\mathbf{p}}^F \cdot \mathbf{w}_F \geq 0,$$

where $\mathbf{T} := \mathbf{T}^S + \mathbf{T}^F$ defines the overall stress of the model, when lingering flow conditions are assumed inside the tissue.

In order to include the electro-chemical effects while the tissue is deforming, it is necessary to derive an equation describing the extensive change of the number of the fixed negative charges via an intensive concentration measure. As the fixed charges almost behave like dissolved ions when they are surrounded by a pore fluid, the molar concentration c_m^{fc} of the fixed charges is introduced, relating the molar number of charges to the surrounding fluid volume. In this regard, we do not distinguish between the intra- and extrafibrillar fluid compartments and relate the fixed charges φ^{fc} to the total local fluid volume knowing well that this may lead to an overestimate in the AF with its high collagen content (Schröder et al. 2007). Following this, two different densities can be introduced for the fixed charges, one relating to the fluid volume, ρ_F^{fc}, and the other one relating to the overall volume of the aggregate, ρ^{fc}. Making use of the constant molar mass of a single fixed negative charge, i.e., the molar mass of an electron $M_m^{fc} \approx 5.486 \times 10^{-7}$ kg/mol, the following relations become obvious

$$\rho^{fc} =: n^F \rho_F^{fc} = n^F c_m^{fc} M_m^{fc}. \qquad (6)$$

Bearing in mind that the fixed charges are attached to the solid skeleton and thus, undergo the same movement, the mass balance of the fixed charge density ρ^{fc} is applied with respect to the deforming solid yielding

$$(\rho^{fc})'_S + \rho^{fc}\, \mathrm{div}\, \mathbf{x}'_S = 0, \qquad (7)$$

or after insertion of (6) and dividing by the constant molar mass M_m^{fc}

$$(n^F c_m^{fc})'_S + n^F c_m^{fc}\, \mathrm{div}\, \mathbf{x}'_S = 0. \qquad (8)$$

Following this, the volume balance (4)$_1$ of the solid skeleton for $\alpha = S$ as well as the concentration balance (8) can be analytically integrated

$$n^S = n_{0S}^S\, \mathrm{det}\, \mathbf{F}_S^{-1},$$
$$c_m^{fc} = c_{0S}^{fc} n_{0S}^F (\mathrm{det}\, \mathbf{F}_S - n_{0S}^S)^{-1} \qquad (9)$$

from an initial solidity n_{0S}^S, porosity n_{0S}^F, and molar concentration c_{0S}^{fc}, respectively. Herein, the latter relation can be understood as an evolution equation for the concentration of the fixed charges needed for the postulation of a constitutive equation used to compute the osmotic pressure contribution.

4 Constitutive assumptions

In order to close the set of governing equations, certain constitutive assumptions for the *Helmholtz* free energies ψ^α, the partial *Cauchy* stress tensors $\mathbf{T}^\alpha$ as well as the interaction term $\hat{\mathbf{p}}^F = -\hat{\mathbf{p}}^S$ need to be defined. In this regard, the chosen constitutive equations must reflect the material behaviour in a best possible manner, thereby embracing anisotropic and viscoelastic effects, the viscous fluid flow as well as the electro-chemical couplings yielding the osmotic pressure contribution.

4.1 Saturation constraint and entropy inequality

Proceeding from general thermodynamical considerations, (Ehlers 1993), a *Lagrange*an multiplier $\mathcal{P}$ is introduced in the sense of an incompressibility constraint. This becomes clear, when the material time derivative of the saturation constraint (1) is taken with respect to the deforming solid. Utilisation of (4)$_1$ yields a continuity like condition

$$-\mathcal{P}[(n^S)'_S + (n^F)'_S] = \mathcal{P}\left[n^S \mathrm{div}\, \mathbf{x}'_S + n^F \mathrm{div}\, \mathbf{x}'_F \right.$$
$$\left. + \mathrm{grad}\, n^F \cdot \mathbf{w}_F \right] = 0, \qquad (10)$$

which is then added to the *Clausius–Planck* inequality (5)$_3$ yielding

$$(\mathbf{T}^S + n^S \mathcal{P}\, \mathbf{I}) \cdot \mathbf{L}_S - \rho^S (\psi^S)'_S$$
$$+ (\mathbf{T}^F + n^F \mathcal{P}\, \mathbf{I}) \cdot \mathbf{L}_F - \rho^F (\psi^F)'_F$$
$$- (\hat{\mathbf{p}}^F - \mathcal{P}\, \mathrm{grad}\, n^F) \cdot \mathbf{w}_F \geq 0. \qquad (11)$$

Herein, use was made of the relation $\mathrm{div}\, \mathbf{x}'_\alpha = \mathbf{L}_\alpha \cdot \mathbf{I}$, where $\mathbf{I}$ denotes the identity tensor. Hence, the partial quantities $\mathbf{T}^\alpha$ and $\hat{\mathbf{p}}^F$ are split into an undetermined part resulting from $\mathcal{P}$ and a so-called extra term $(\cdot)_E$ to be determined via appropriate constitutive equations, viz.

$$\mathbf{T}^\alpha = -n^\alpha \mathcal{P}\, \mathbf{I} + \mathbf{T}_E^\alpha \quad \text{and} \quad \hat{\mathbf{p}}^F = \mathcal{P}\, \mathrm{grad}\, n^F + \hat{\mathbf{p}}_E^F. \qquad (12)$$

The overall *Cauchy* stress of the model is simply obtained by a summation of the partial stresses under utilisation of (1) such that

$$\mathbf{T} = -\mathcal{P}\, \mathbf{I} + \mathbf{T}_E \quad \text{with } \mathbf{T}_E = \mathbf{T}_E^S + \mathbf{T}_E^F, \qquad (13)$$

where according to Bishop (1959) or Skempton (1960), $\mathbf{T}_E$ is known as the effective or extra stress. Hence, $\mathcal{P}$ is easily identified as the unspecified hydraulic pore pressure, whereas

the extra stress is purely governed by an electro-chemical contribution, the deformation state as well as the fluid viscosity and velocity.

4.2 Effective stress of the fluid and solid constituent

As a usual assumption in hydraulics, the fluid extra stress is neglected (i.e., $\mathbf{T}_E^F \approx \mathbf{0}$) in comparison with the extra momentum production term $\hat{\mathbf{p}}_E^F$, which is responsible for the drag force resulting from the percolating fluid. This fact can be deduced from an order-of-magnitude analysis, see, e.g., Hassanizadeh and Gray (1987), Ehlers et al. (1999) or Markert (2007) and quotations therein. Moreover, concerning the incompressible fluid constituent, it can be shown that the set of constitutive variables for the free energy function is empty, i.e., its free energy $\psi^F = \psi^F(\cdot)$ is constant (Ehlers 2002).

The remaining undetermined solid extra stress is then further split into an osmotic and a mechanical contribution. The reason for this split becomes clear, when the physical effect of the attached negative fixed charges of the ECM on the behaviour of the overall tissue is analysed. Herein, a phenomenon called osmosis is activated, which results in a spontaneous fluid movement across the tissue boundary. In this context, the fluid will flow from places with lower solute concentration to regions with higher concentrations, thereby dilating the tissue. As the incompressible fluid constituent is assumed to be non-sensitive to changes in porosity n^F, the volume dilatation is solely carried via tension in the solid matrix. This is due to the fact that an externally applied hydrostatic pore pressure is constant in an incompressible fluid, no matter how much space (i.e., n^F) is available for the pore-fluid. The osmosis-driven inflow of fluid takes place until it is balanced with the outflow of fluid resulting from the "squeezing force" of the dilated solid matrix. Finally, the tension in the ECM at osmotic equilibrium is then defined as the osmotic pressure difference $\Delta\pi$ contributing to the hydrostatic stress state. Thus, the solid extra stress is further split, viz.

$$\mathbf{T}_E^S = \mathbf{T}_{E,\,\text{OSM}}^S + \mathbf{T}_{E,\,\text{MECH}}^S, \quad \text{where } \mathbf{T}_{E,\,\text{OSM}}^S = -\Delta\pi\,\mathbf{I}. \tag{14}$$

Moreover, concerning the purely mechanical behaviour of the anisotropic and viscoelastic ECM, another additive concept is assumed yielding

$$\mathbf{T}_{E,\text{MECH}}^S = \mathbf{T}_{\text{ISO}}^S + \mathbf{T}_{\text{ANISO}}^S \quad \text{with } \mathbf{T}_{\text{ISO}}^S = \mathbf{T}_{\text{EQ}}^S + \mathbf{T}_{\text{NEQ}}^S, \tag{15}$$

where the respective mechanical *Cauchy* stress is split into an isotropic (PGs, GAGs, etc.) and an anisotropic (oriented collagen of type I) contribution. In this regard, the isotropic part is further split into equilibrium and non-equilibrium parts accounting for the intrinsic viscoelastic behaviour of the isotopic fraction of the ECM.
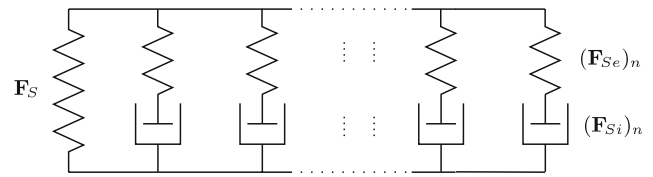

Fig. 2 Generalised *Maxwell* model composed of a spring-element and n *Maxwell* elements

4.3 Inelastic solid kinematics

In order to describe finite viscoelasticity, it is convenient to proceed from a generalised *Maxwell* model as depicted in Fig. 2 and described in Ehlers et al. (2002), Markert (2005) or Reese and Govindjee (1998), which accounts for the purely elastic equilibrium (EQ) stress via its elastic spring as well as for the non-equilibrium (NEQ) overstresses via the respective $n = 1, \ldots, N$ *Maxwell* branches.

As usual in finite inelasticity, the model is constitutively based on a multiplicative split of the solid deformation gradient $\mathbf{F}_S = (\mathbf{F}_{Se})_n (\mathbf{F}_{Si})_n$ into inelastic deformations $(\mathbf{F}_{Si})_n$ operating between the reference and the stress-free intermediate configurations of the nth *Maxwell* element as well as elastic deformations $(\mathbf{F}_{Se})_n$ connecting the respective nth intermediate configuration with the actual frame. In this context, an additive decomposition of the resulting finite strain measures into elastic and inelastic parts is achieved (Lee 1969; Kleiber 1975; Ehlers 1989, 1991, 1993)

$$\mathbf{E}_S = \frac{1}{2}(\mathbf{C}_S - \mathbf{I}), \quad (\mathbf{E}_{Si})_n = \frac{1}{2}[(\mathbf{C}_{Si})_n - \mathbf{I}],$$
$$(\mathbf{E}_{Se})_n = \mathbf{E}_S - (\mathbf{E}_{Si})_n = \frac{1}{2}[\mathbf{C}_S - (\mathbf{C}_{Si})_n], \tag{16}$$

directly reflecting the structure of the underlying rheological model given in Fig. 2. Herein, $\mathbf{E}_S$, $(\mathbf{E}_{Si})_n$, and $(\mathbf{E}_{Se})_n$ are the respective total, inelastic and elastic *Green-Lagrange*an strains, which are defined in the reference configuration. Note in passing that

$$(\widehat{\boldsymbol{\Gamma}}_{Se})_n = (\mathbf{F}_{Si}^{T-1})_n (\mathbf{E}_{Se})_n (\mathbf{F}_{Si}^{-1})_n = \frac{1}{2}[(\widehat{\mathbf{C}}_{Se})_n - \mathbf{I}] \tag{17}$$

are the associate elastic strain measures defined on the intermediate configurations of the respective *Maxwell* branches, subsequently denoted by $(\widehat{\cdot})$, and can be computed via an inelastic push-forward of $(\mathbf{E}_{Se})_n$ (Ehlers 1989, 1991, 1993). In this regard, the intermediate configurations can be understood as the reference configurations of the springs in the *Maxwell* branches. Moreover, the respective right *Cauchy-Green* deformation tensors are defined as

$$\mathbf{C}_S = \mathbf{F}_S^T\,\mathbf{F}_S, \quad (\widehat{\mathbf{C}}_{Se})_n = (\mathbf{F}_{Se}^T)_n\,(\mathbf{F}_{Se})_n,$$
$$(\mathbf{C}_{Si})_n = (\mathbf{F}_{Si}^T)_n\,(\mathbf{F}_{Si})_n. \tag{18}$$

4.4 Entropy principle for viscoelastic solid skeleton

As a next step, the modified *Clausius–Planck* inequality (11) has to be evaluated in order to achieve rules for the computation of the solid extra stress as well as restrictions for the evolution equations of the internal variables. Proceeding from an incompressible fluid at thermodynamical equilibrium, i.e., $[\psi^F(\cdot)]'_F = 0$ and $\mathbf{T}_E^F \equiv \mathbf{0}$, respectively, the inequality (11) is evaluated using the conjugate pair of the solid stress power in the referential frame,

$$\mathbf{S}_E^S \cdot (\mathbf{E}_S)'_S - \rho_{0S}^S (\psi^S)'_S - \hat{\mathbf{p}}_E^F \cdot \mathbf{w}_F \geq 0\,, \tag{19}$$

where $\mathbf{S}_E^S$ is the second *Piola–Kirchhoff* solid extra stress. Due to the fundamental principles of constitutive modelling, cf. Noll (1958) and Truesdell (1949), namely determinism, local action and equipresence, the solid *Helmholtz* free energy ψ^S may depend on the solid deformation gradient $\mathbf{F}_S$ as well as on some second-order structural tensors $\boldsymbol{\mathcal{M}}^S$ characterising the kind of anisotropy. In view of the fact that the free energy can only be stored as an elastic potential in the spring elements, the non-equilibrium parts of the *Maxwell* elements have to depend on $(\mathbf{F}_{Se})_n$. Thus, the suggested split of ψ^S yields osmotic (ψ_{OSM}^S), equilibrium (ψ_{EQ}^S), and anisotropic (ψ_{ANISO}^S) contributions, each associated with the total deformation $\mathbf{F}_S$, as well as a non-equilibrium part (ψ_{NEQ}^S) explicitly depending on the elastic deformations $(\mathbf{F}_{Se})_n$ of the *Maxwell* branches, thereby including an implicit dependence on the internal variables $(\mathbf{F}_{Si})_n$, as the respective time-dependent dashpot deformations influence the elastic deformation gradient.

Recalling the arguments stemming from the concept of material frame indifference (objectivity), the respective deformation gradients are not admissible as process variables and have to be replaced by the set of deformation tensors (18), or according to (16) by the corresponding strain measures. Proceeding from the definition of a strain-energy function $W^S = \rho_{0S}^S \psi^S$ representing the stored elastic energy defined per unit reference volume, the stress power in the referential frame evolves as

$$(W^S)'_S = \left[\frac{\partial W_{\text{OSM}}^S}{\partial \mathbf{E}_S} + \frac{\partial W_{\text{EQ}}^S}{\partial \mathbf{E}_S} + \frac{\partial W_{\text{ANISO}}^S}{\partial \mathbf{E}_S} \right] \cdot (\mathbf{E}_S)'_S$$
$$+ \sum_{n=1}^N \frac{\partial W_{\text{NEQ}}^S}{\partial (\mathbf{E}_{Se})_n} \cdot [(\mathbf{E}_{Se})_n]'_S\,. \tag{20}$$

The implicit dependence of W_{NEQ}^S on the inelastic deformations $(\mathbf{F}_{Si})_n$ is identified, when the derivative of the non-equilibrium part is rewritten with the aid of the inelastic push-forward used in Eq. (17) yielding

$$\frac{\partial W_{\text{NEQ}}^S}{\partial \mathbf{E}_{Se}} = \left(\frac{\partial \widehat{\boldsymbol{\Gamma}}_{Se}}{\partial \mathbf{E}_{Se}} \right)^T \frac{\partial W_{\text{NEQ}}^S}{\partial \widehat{\boldsymbol{\Gamma}}_{Se}}$$
$$= \left[\frac{\partial (\mathbf{F}_{Si}^{T-1} \mathbf{E}_{Se} \mathbf{F}_{Si}^{-1})}{\partial \mathbf{E}_{Se}} \right]^T \frac{\partial W_{\text{NEQ}}^S}{\partial \widehat{\boldsymbol{\Gamma}}_{Se}}$$
$$= \mathbf{F}_{Si}^{-1} \frac{\partial W_{\text{NEQ}}^S}{\partial \widehat{\boldsymbol{\Gamma}}_{Se}} \mathbf{F}_{Si}^{T-1}\,, \tag{21}$$

carried out in an exemplary way using $N = 1$. The latter part of (21) clearly reveals that the non-equilibrium strain energy depends explicitly on the elastic strain, while the inelastic push-forward $\mathbf{F}_{Si}^{-1}(\cdot)\mathbf{F}_{Si}^{T-1}$ is associated with the movement of the time-dependent position of the inelastic intermediate configuration. Thus, in regard of an iterative numerical implementation, the need for evolution equations of the internal variables $(\mathbf{F}_{Si})_n$ or $(\mathbf{C}_{Si})_n$ becomes clear.

Inserting Eqs. (20) and (21) into the inequality (19) as well as utilising the material time derivative $[(\mathbf{E}_{Se})_n]'_S = (\mathbf{E}_S)'_S - [(\mathbf{E}_{Si})_n]'_S$ stemming from Eq. (16)$_3$, finally yields an expression for the determination of the solid extra stress $\mathbf{S}_E^S$,

$$\left[\mathbf{S}_E^S - \underbrace{\frac{\partial W_{\text{OSM}}^S}{\partial \mathbf{E}_S}}_{\mathbf{S}_{\text{OSM}}^S} - \underbrace{\frac{\partial W_{\text{EQ}}^S}{\partial \mathbf{E}_S}}_{\mathbf{S}_{\text{EQ}}^S} - \sum_{n=1}^N \underbrace{\overbrace{(\mathbf{F}_{Si}^{-1})_n \frac{\partial W_{\text{NEQ}}^S}{\partial (\widehat{\boldsymbol{\Gamma}}_{Se})_n} (\mathbf{F}_{Si}^{T-1})_n}^{\mathbf{S}_n^S}}_{\mathbf{S}_{\text{NEQ}}^S} \right.$$
$$\left. - \underbrace{\frac{\partial W_{\text{ANISO}}^S}{\partial \mathbf{E}_S}}_{\mathbf{S}_{\text{ANISO}}^S} \right] \cdot (\mathbf{E}_S)'_S = 0 \quad \forall (\mathbf{E}_S)'_S, \tag{22}$$

where $\mathbf{S}_n^S$ is the non-equilibrium stress of a single *Maxwell* element and $\mathbf{S}_{\text{NEQ}}^S$ is the sum of the generalised model. The remainder of (19) is known as dissipation inequality

$$\sum_{n=1}^N \left(\mathbf{F}_{Si}^{-1} \right)_n \frac{\partial W_{\text{NEQ}}^S}{\partial (\widehat{\boldsymbol{\Gamma}}_{Se})_n} (\mathbf{F}_{Si}^{T-1})_n \cdot [(\mathbf{E}_{Si})_n]'_S - \hat{\mathbf{p}}_E^F \cdot \mathbf{w}_F \geq 0$$
$$\forall \left\{ [(\mathbf{E}_{Si})_n]'_S, \mathbf{w}_F \right\}\,, \tag{23}$$

which is needed to derive the evolution equations for the internal variables $(\mathbf{F}_{Si})_n$ or $(\mathbf{C}_{Si})_n$ as well as the constitutive assumption for the fluid momentum production $\hat{\mathbf{p}}_E^F$. Finally, the *Cauchy* extra stress $\mathbf{T}_E^S$ and the *Kirchoff* extra stress $\boldsymbol{\tau}_E^S$ can be computed applying a push-forward operation to the second *Piola–Kirchhoff* stress such that

$$\boldsymbol{\tau}_E^S = \mathbf{F}_S \mathbf{S}_E^S \mathbf{F}_S^T \text{ and } \mathbf{T}_E^S = \det \mathbf{F}_S^{-1} \boldsymbol{\tau}_E^S\,. \tag{24}$$

4.5 Dissipation of the viscous solid skeleton

In order to derive the evolution equation for the chosen internal variables $(\mathbf{C}_{Si})_n$, the solid part of the dissipation inequality (23) is expressed in terms of the respective intermediate configuration as the current configuration of the inelastic process. This is done, because one describes the dissipation process of the solid material using real quantities on its actual (i.e., intermediate) configuration rather than using the image of these quantities in the reference configuration. Having in mind the push-forward $(24)_1$, it is easily concluded that a similar transport with the inelastic part of the deformation gradient yields the intermediate-state overstress tensor of a *Maxwell* branch

$$\widehat{\boldsymbol{\tau}}_n^S = (\mathbf{F}_{Si})_n\,(\mathbf{S}_n^S)\,(\mathbf{F}_{Si}^T)_n\,. \tag{25}$$

Note that the computation of an entire intermediate-state overstress tensor $\widehat{\boldsymbol{\tau}}_{\text{NEQ}}^S$ is only possible in the case of $N = 1$, as the individual intermediate overstresses of more than one *Maxwell* element may operate on different intermediate configurations. For $N \geq 1$, a summation has to be carried out on the referential or the actual configuration using $\mathbf{S}_n^S$ or $\boldsymbol{\tau}_n^S$, respectively. Hence, the first part of the dissipation inequality (23) has to be evaluated in a mathematically sufficient sense for every *Maxwell* element and can be rewritten as

$$\widehat{\boldsymbol{\tau}}_n^S \cdot (\mathbf{F}_{Si}^{T-1})_n\,[(\mathbf{E}_{Si})_n]_S'\,(\mathbf{F}_{Si}^{-1})_n = \widehat{\boldsymbol{\tau}}_n^S \cdot (\widehat{\mathbf{D}}_{Si})_n \geq 0\,, \tag{26}$$

where $(\widehat{\mathbf{D}}_{Si})_n$ are the respective symmetric deformation velocity tensors of the intermediate configurations. This inequality is sufficiently satisfied with the simple ansatz

$$(\widehat{\mathbf{D}}_{Si})_n \propto \widehat{\boldsymbol{\tau}}_n^S \longrightarrow (\widehat{\mathbf{D}}_{Si})_n = \frac{1}{2\eta_n^S}\,\widehat{\boldsymbol{\tau}}_n^S$$

$$-\frac{\zeta_n^S}{2\eta_n^S(2\eta_n^S + 3\zeta_n^S)}(\widehat{\boldsymbol{\tau}}_n^S \cdot \mathbf{I})\mathbf{I}, \tag{27}$$

where η_n^S and ζ_n^S are the macroscopic shear and bulk viscosities of the dashpot in a *Maxwell* element, respectively. In this context, relation $(27)_2$ is the inverse from the well-known stress–strain rate relation for a dashpot yielding a linear relation between $\widehat{\boldsymbol{\tau}}_n^S$ and $(\widehat{\mathbf{D}}_{Si})_n$ (Markert 2005). Since inequality (26) has to be satisfied, it is easily concluded, that the restrictions on the viscosities $\eta_n^S > 0$ and $2\,\eta_n^S + 3\,\zeta_n^S > 0$ must hold. However, with regard to the numerical evaluation of the evolution equation, it is most convenient, when the spatio-temporal discretisation of $(27)_2$ is carried out on the constant reference configuration. Applying the known transport mechanisms for $\widehat{\mathbf{D}}_{Si}$ described in (26) as well as for $\widehat{\boldsymbol{\tau}}_n^S$ in (25) yields the final form of the evolution equation

$$[(\mathbf{C}_{Si})_n]_S' - \frac{1}{\eta_n^S}\,(\mathbf{C}_{Si})_n\,\mathbf{S}_n^S\,(\mathbf{C}_{Si})_n + \frac{\zeta_n^S}{\eta_n^S\,(2\,\eta_n^S + 3\,\zeta_n^S)}$$

$$[\mathbf{S}_n^S \cdot (\mathbf{C}_{Si})_n]\,(\mathbf{C}_{Si})_n = \mathbf{0}\,, \tag{28}$$

where the chosen internal variables $(\mathbf{C}_{Si})_n$ appear in an explicit manner, when integrated using a backward *Euler* scheme.

4.6 Dissipation of the viscous interstitial fluid

Finally, the remaining unspecified extra quantity $\hat{\mathbf{p}}_E^F$ needs to be defined by an appropriate constitutive law reflecting the properties of a viscous interstitial fluid. Inserting the constitutive assumption $\hat{\mathbf{p}}_E^F = -(n^F)^2\,(\mathbf{K}^F)^{-1}\,\mathbf{w}_F$ into Eq. (12) and then into the fluid momentum balance $(4)_2$ leads to the well known *Darcy* filter law

$$n^F\mathbf{w}_F = -\mathbf{K}^F\,(\text{grad}\,\mathcal{P} - \rho^{FR}\,\mathbf{b})\quad \text{with}\ \mathbf{K}^F = \frac{K^S}{\mu^{FR}}\mathbf{I} \tag{29}$$

relating the hydraulic pressure gradient to the filter velocity $n^F\mathbf{w}_F$ via the *Darcy* permeability tensor $\mathbf{K}^F$. In this context, K^S is the intrinsic permeability, which is solely a measure of the pore geometry, and $\mu^{FR} > 0$ is the effective fluid viscosity. A deformation dependence can be introduced for the intrinsic permeability which, according to Markert (2007), can be computed using

$$K^S = K_{0S}^S\left(\frac{J_S - n_{0S}^S}{n_{0S}^F}\right)^\kappa. \tag{30}$$

Herein, K_{0S}^S is the initial permeability of the undeformed tissue and $\kappa \geq 0$ is a parameter governing the non-linearity of the deformation dependency. Note that $\kappa = 0$ turns off the deformation dependency. Moreover, due to the positive definiteness of $\mathbf{K}^F$, the remaining fluid part of the entropy inequality (19) is satisfied for $K_{0S}^S > 0$.

4.7 General structure of the solid strain energy

Regarding the definition of constitutive equations describing the respective parts of W^S, it is advantageous to a priori define a general structure to be used. Starting with the osmotic part, the beginning of the section states that osmosis triggers a variation of the volume which is occupied by the incompressible pore-fluid. In this regard, a purely volumetric deformation can be initiated in the case of purely isotropic material behaviour, which is accompanied by shape changes in the case of an anisotropic behaviour resulting from the presence of collagen fibres. Following this, the most suitable process variable would be $\det \mathbf{F}_S = (\det \mathbf{C}_S)^{\frac{1}{2}}$ which describes the local dilatation of the ECM. The change in shape may then be caused by the anisotropic stress response of the material. Moreover, the solid strain energy functions are often formulated in a very general way using the principal stretches of the deformation. In this regard and in order to adopt the results of the classical mechanics of single phase materials, the process variables of choice are $\mathbf{C}_S$ and $(\widehat{\mathbf{C}}_{Se})_n$.

This allows for the conclusive form

$$W^S = W^S_{\text{OSM}}(\det \mathbf{C}_S) + W^S_{\text{EQ}}(\mathbf{C}_S) + \sum_{n=1}^{N} W^S_{\text{NEQ}}[(\widehat{\mathbf{C}}_{Se})_n]$$
$$+ W^S_{\text{ANISO}}(\mathbf{C}_S, \boldsymbol{\mathcal{M}}^S) . \tag{31}$$

Applying the chain rule to Eqs. $(16)_1$ and (17), the stress computation concluded from Eq. (22) can be rewritten in terms of the actual configuration yielding the *Kirchhoff* stress

$$\boldsymbol{\tau}^S_E = \underbrace{2 \, \mathbf{F}_S \frac{\partial W^S_{\text{OSM}}}{\partial \mathbf{C}_S} \mathbf{F}^T_S}_{\boldsymbol{\tau}^S_{\text{OSM}}} + \underbrace{2 \, \mathbf{F}_S \frac{\partial W^S_{\text{EQ}}}{\partial \mathbf{C}_S} \mathbf{F}^T_S}_{\boldsymbol{\tau}^S_{\text{EQ}}}$$

$$+ 2 \sum_{n=1}^{N} \overbrace{(\mathbf{F}_{Se})_n \frac{\partial W^S_{\text{NEQ}}}{\partial (\widehat{\mathbf{C}}_{Se})_n} (\mathbf{F}^T_{Se})_n}^{\boldsymbol{\tau}^S_n} + \underbrace{2 \, \mathbf{F}_S \frac{\partial W^S_{\text{ANISO}}}{\partial \mathbf{C}_S} \mathbf{F}^T_S}_{\boldsymbol{\tau}^S_{\text{ANISO}}} .$$
$$\underbrace{}_{\boldsymbol{\tau}^S_{\text{NEQ}}}$$
$$\tag{32}$$

4.8 Specific solid strain energies

As a final step, the respective solid strain energies need to be defined, which is achieved by the concept of scalar-valued isotropic tensor functions. Starting with the osmotic contribution, a volumetric strain energy is postulated by use of $(9)_2$ together with the relation $\det \mathbf{F}_S = (\det \mathbf{C}_S)^{\frac{1}{2}}$ yielding

$$W^S_{\text{OSM}}[c^{fc}_m(\det \mathbf{C}_S)] = R \, \Theta \, c^{fc}_{0S} \, n^F_{0S}$$

$$\left[\frac{2 \, \bar{c}_m}{c^{fc}_m} - \frac{\sqrt{4 \, \bar{c}^2_m + (c^{fc}_m)^2}}{c^{fc}_m} + \text{arsinh} \left(\frac{c^{fc}_m}{2 \, \bar{c}_m} \right) \right] ,$$

$$\text{where } c^{fc}_m = c^{fc}_{0S} n^F_{0S} \left[(\det \mathbf{C}_S)^{\frac{1}{2}} - n^S_{0S} \right]^{-1} . \tag{33}$$

Herein, R denotes the universal gas constant, Θ is the absolute temperature, whereas $\bar{c}_m$ is the molar concentration of the external monovalent solution surrounding the tissue, which can be treated as a material parameter. In this regard, $(33)_1$ yields the scalar-valued function relating the osmotic pressure difference $\Delta\pi$ to the concentration differences between the pore fluid and the external solution. Hence, (33) in combination with $(24)_2$ and (32) is equivalent to the classical way, where one proceeds from the simple example of a reservoir filled with two solutions of different concentrations being separated by a semi-permeable membrane. Following this approach, *van't Hoff*'s osmotic law can be applied yielding the osmotic pressure difference of the two chemically active solutions at the semi-permeable membrane:

$$\mathbf{T}^S_{E,\text{OSM}} = \det \mathbf{F}^{-1}_S \, \boldsymbol{\tau}^S_{E,\text{OSM}} = -\Delta\pi \, \mathbf{I},$$
$$\text{where } \Delta\pi = R\Theta \left[(c^+_m + c^-_m) - (\bar{c}^+_m + \bar{c}^-_m) \right] . \tag{34}$$

Herein, c^γ_m and $\bar{c}^\gamma_m$ for $\gamma = +, -$ are the molar solute concentrations (i.e., anions and cations) of the internal and external solutions, respectively. Following this, the concentrations of one solution can be prescribed in the sense of a boundary condition, while the concentrations of the other solution may be determined using the Donnan (1911) equation,

$$c^+_m c^-_m = \bar{c}^+_m \bar{c}^-_m , \tag{35}$$

which provides the chemical equilibrium at the semi-permeable membrane. Applying this concept to the IVD means firstly that the two solutions will be referred to as internal and external (surrounding) solutions while the semi-permeable membrane must be understood as the boundary surface of the IVD. Note in passing that exploiting the Lanir (1987) assumption allows to extend the applicability of Eq. (35) from the domain boundary to the whole IVD. Secondly, it is crucial to incorporate the fixed negative charges as they contribute to the ion-concentration of the internal solution yielding the osmotic effect. Hence, the electro-neutrality condition needs to be applied, thereby always ensuring enough cations being left to balance out the fixed negative charges. In this context, the following relations hold for the external and internal solutions, respectively

$$z^+ \bar{c}^+_m + z^- \bar{c}^-_m = 0 \longrightarrow \bar{c}^-_m = \bar{c}^+_m =: \bar{c}_m$$
$$\quad \text{(external solution)},$$
$$z^+ c^+_m + z^- c^-_m + z^{fc} c^{fc}_m = 0 \longrightarrow c^-_m = c^+_m - c^{fc}_m$$
$$\quad \text{(internal solution)}. \tag{36}$$

Therein, the corresponding valences were used for a monovalent salt solution (i.e., Na^+Cl^-) reading $z^+ = 1$ and $z^- = z^{fc} = -1$. Inserting the results of Eqs. (36) into the *Donnan* equation (35) yields the two relations

$$c^+_m = \sqrt{\bar{c}^2_m + \left(\frac{c^{fc}_m}{2} \right)^2} + \frac{c^{fc}_m}{2} \quad \text{and}$$

$$c^-_m = \sqrt{\bar{c}^2_m + \left(\frac{c^{fc}_m}{2} \right)^2} - \frac{c^{fc}_m}{2} \tag{37}$$

also known as the *Donnan* equilibrium. Finally, the constitutive equation for the osmotic pressure (i.e., osmotic pressure caused by large molecules, such as PGs and GAGs) can be postulated by inserting Eqs. (37) and $(36)_1$ into (34) and $(14)_2$ yielding

$$\mathbf{T}^S_{E,\text{OSM}} = -\Delta\pi \, \mathbf{I} = -2R \, \Theta \left[\sqrt{\bar{c}^2_m + (c^{fc}_m/2)^2} - \bar{c}_m \right] \mathbf{I},$$
$$\tag{38}$$

where c^{fc}_m is deformation dependent as seen in equation $(9)_2$.

In order to keep the model as general as possible, an *Ogden* ansatz is chosen for the mechanical equilibrium and non-equilibrium strain-energies, thereby allowing for the simulation of any complexity level ranging from very simple to highly non-linear material behaviour

$$
W_{\text{EQ}}^S = \mu_0^S \sum_{m=1}^{M_0} \left[\sum_{k=1}^{3} \frac{\mu_{0(m)}^*}{\alpha_{0(m)}} \left(\lambda_{S(k)}^{\alpha_{0(m)}/2} - 1 \right) \right.
$$
$$
\left. - \mu_{0(m)}^* \ln (J_S) \right] + U_{\text{EQ}}^S(J_S),
$$
$$
(39)
$$
$$
W_{\text{NEQ}}^S = \sum_{n=1}^{N} \mu_n^S \sum_{m=1}^{M_n} \left[\sum_{k=1}^{3} \frac{\mu_{n(m)}^*}{\alpha_{n(m)}} \left((\lambda_{Se(k)}^{\alpha_{n(m)}/2})_n - 1 \right) \right.
$$
$$
\left. - \mu_{n(m)}^* \ln (J_{Se})_n \right] + U_{\text{NEQ}}^S[(J_{Se})_n].
$$

Herein, $\lambda_{S(k)}$ and $(\lambda_{Se(k)})_n$ for $k = 1, 2, 3$ denote the eigenvalues of the right $\mathbf{C}_S$ and $(\mathbf{C}_{Se})_n$ or the left $\mathbf{B}_S$ and $(\mathbf{B}_{Se})_n$ deformation tensors, respectively. The *Jacobi*ans are defined as $J_S = \det \mathbf{F}_S$ and $(J_{Se})_n = \det (\mathbf{F}_{Se})_n$, and the indices m and k denote the number of *Ogden* terms to be taken and the dimension in space, respectively. Moreover, $\mu_0^S > 0$ and $\mu_n^S > 0$ are the first *Lamé* constants, i.e., the classical ground-state shear moduli, whereas $\mu_{0(m)}^*$, $\mu_{n(m)}^*$, $\alpha_{0(m)}$, and $\alpha_{n(m)}$ represent dimensionless, real-valued material parameters. By making specific choices of the parameters M, μ_m^* and α_m

Model	M	μ_m^*	α_m
Varga	1	$\mu_1^* = 2$	$\alpha_1 = 1$
neo-*Hooke*	1	$\mu_1^* = 1$	$\alpha_1 = 2$
Mooney–Rivlin	2	$\mu_1^* - \mu_2^* = 1$	$\alpha_1 = 2, \alpha_2 = -2$

$$
(40)
$$

it turns out that the *Ogden* law (39) comprises other well-known finite elasticity models, such as the *Varga*, neo-*Hooke*, or *Mooney–Rivlin* model (Mooney 1940; Rivlin 1948; Varga 1966; Treloar 1975). Since the strain energies (39) describe a porous material, a volumetric response function needs to be defined in order to ensure the compaction point, which is reached when there is no pore space left. However, due to the very small permeability of soft biological tissues in general, the volumetric response function mainly serves to limit the dilatation of the ECM, as the compaction point is rarely reached. Thus, the volumetric extension can be taken in accordance to Eipper (1998), viz.

$$
U_{\text{EQ}}^S = \frac{\Lambda_0^S}{\gamma_0^S \left(\gamma_0^S - 1 + \frac{1}{(1-n_{0S}^S)^2} \right)}
$$
$$
\left(J_S^{\gamma_0^S} - 1 - \gamma_0^S \ln \frac{J_S - n_{0S}^S}{1 - n_{0S}^S} + \gamma_0^S n_{0S}^S \frac{J_S - 1}{1 - n_{0S}^S} \right),
$$
$$
U_{\text{NEQ}}^S = \sum_{n=1}^{N} \frac{\Lambda_n^S}{\gamma_n^S \left(\gamma_n^S - 1 + \frac{1}{[1-(n_{Si}^S)_n]^2} \right)} \qquad (41)
$$
$$
\left((J_{Se}^{\gamma_n^S})_n - 1 - \gamma_n^S \ln \frac{(J_{Se})_n - (n_{Si}^S)_n}{1 - (n_{Si}^S)_n} \right.
$$
$$
\left. + \gamma_n^S n_{Si}^S \frac{(J_{Se})_n - 1}{1 - (n_{Si}^S)_n} \right).
$$

Herein, $\Lambda_0^S > 0$ and $\Lambda_n^S > 0$ are the second *Lamé* constants, whereas $\gamma_0^S > 1$ and $\gamma_n^S > 1$ are dimensionless material parameters governing the non-linearity of the volumetric extension terms. Moreover, the inelastic solidities $(n_{Si}^S)_n := n_{0S}^S (J_{Si}^{-1})_n$ are introduced with the aid of the inelastic *Jacobi*an determinants $(J_{Si}^{-1})_n = \det (\mathbf{F}_{Si})_n$.

The anisotropic contribution of the strain-energy function describing the locally orthotropic fibre reinforcements (Markert et al. 2005) can be postulated following a similar polynomial concept as is used in the *Ogden*-ansatz yielding

$$
W_{\text{ANISO}}^S = \sum_{q=1}^{M_f} \left[\frac{\tilde{\mu}_q^S}{\tilde{\gamma}_q^S} (\mathrm{I}_4^{\tilde{\gamma}_q^S/2} + \mathrm{I}_6^{\tilde{\gamma}_q^S/2} - 2) \right.
$$
$$
\left. - \tilde{\mu}_q^S \ln (\mathrm{I}_4 \mathrm{I}_6)^{1/2} \right] \forall \mathrm{I}_4, \mathrm{I}_6 \geq 1. \qquad (42)
$$

Therein, M_f denotes the number of polynomials to be used, $\tilde{\mu}_q^S$ and $\tilde{\gamma}_q^S$ are material parameters, and

$$
\mathrm{I}_4 = \mathcal{M}_a^S \cdot \mathbf{C}_S = (\mathbf{a}_0 \otimes \mathbf{a}_0) \cdot \mathbf{C}_S = \mathbf{a}_0 \cdot \mathbf{C}_S \mathbf{a}_0,
$$
$$
\mathrm{I}_6 = \mathcal{M}_b^S \cdot \mathbf{C}_S = (\mathbf{b}_0 \otimes \mathbf{b}_0) \cdot \mathbf{C}_S = \mathbf{b}_0 \cdot \mathbf{C}_S \mathbf{b}_0 \qquad (43)
$$

are the mixed invariants describing the squared stretches in the respective fibre directions, thereby having a clear physical interpretation (Spencer 1984). In this context, the unit fibre vectors $\mathbf{a}_0$ and $\mathbf{b}_0$ are defined in the undeformed state. Like in the theory of ropes, the collagen fibres are assumed to carry loads only under tension. Therefore, the restriction $\{\mathrm{I}_4, \mathrm{I}_6\} \geq 1$ must hold, which simultaneously satisfies restrictions stemming from polyconvexity considerations (Balzani et al. 2005; Holzapfel et al. 2004; Schröder and Neff 2003). Note in passing that the equilibrium and non-equilibrium parts also fulfil the polyconvexity requirement, thereby ensuring the existence of minimisers in variational problems appearing in the framework of the finite element method (FEM).

5 Numerical modelling

The FEM has been proven to provide a suitable algorithm to approximate the resulting set of coupled partial differential equations stemming from the extended biphasic solid–fluid model. In this context, the local forms of the governing multi-field equations $(5)_{1,2}$ must be brought into a form suitable for the numerical approximation process. After inserting Eq. (29) into $(5)_1$, the quasi-static model under consideration incorporates two main fields, namely the solid displacement $\mathbf{u}_S$ and the hydraulic pore-fluid pressure $\mathcal{P}$. As the osmotic pressure difference $\Delta\pi$ of the solid extra stress $\mathbf{T}^S_{E,\text{OSM}}$ can be added on the hydraulic pressure $\mathcal{P}$, the entire pressure $p = \Delta\pi + \mathcal{P}$ of the model is introduced.

In regard of the FEM as the chosen variational approximation method, the corresponding local forms of the field equations are transferred into a so-called weak formulation claiming to be fulfilled in an integral sense instead of seeking for a closed-form solution for the strong formulation. Thus, the strong forms $(5)_{1,2}$ are integrated over the spatial domain Ω occupied by the porous tissue at time t. Subsequently, the variational formulation is obtained, when the respective terms are weighted by independent test functions $\delta\mathbf{u}_S$ and $\delta\mathcal{P}$. However, in order to allow the application of boundary conditions, some of the volume integrals have to be transformed into surface integrals. As there are two coupled differential equations, the overall surface $\Gamma = \partial\Omega$ of the domain Ω is mathematically split into

$$
\begin{aligned}
&\Gamma = \Gamma_{\mathbf{u}} \cup \Gamma_{\mathbf{t}} \quad \text{with } \Gamma_{\mathbf{u}} \cap \Gamma_{\mathbf{t}} = \emptyset, \\
&\Gamma = \Gamma_{\mathcal{P}} \cup \Gamma_q \quad \text{with } \Gamma_{\mathcal{P}} \cap \Gamma_q = \emptyset,
\end{aligned}
\tag{44}
$$

where $\Gamma_{\mathbf{u}}$ and $\Gamma_{\mathcal{P}}$ are the *Dirichlet* boundaries for the unknown quantities $\mathbf{u}_S$ and $\mathcal{P}$, while $\Gamma_{\mathbf{t}}$ and Γ_q represent the respective *Neumann* parts. After applying the product rule and the *Gauß*ian integral theorem, the weak formulations for the corresponding balances evolve

$$
\int_\Omega \text{div}\,(\mathbf{u}_S)'_S\,\delta\mathcal{P}\mathrm{d}v + \int_\Omega \left[\frac{K^S}{\mu^{FR}}(\text{grad}\,\mathcal{P} - \rho^{FR}\mathbf{b})\right]\cdot\text{grad}\,\delta\mathcal{P}\mathrm{d}v
$$

$$
+ \int_{\Gamma_q} \bar{q}\delta\mathcal{P}\mathrm{d}a = 0,
$$

$$
\int_\Omega \left(\mathbf{T}^S_{E,\text{MECH}} - p\mathbf{I}\right)\cdot\text{grad}\,\delta\mathbf{u}_S\,\mathrm{d}v
$$

$$
- \int_\Omega \left(n^S\rho^{SR} + n^F\rho^{FR}\right)\mathbf{b}\cdot\delta\mathbf{u}_S\mathrm{d}v - \int_{\Gamma_{\mathbf{t}}} \bar{\mathbf{t}}\cdot\delta\mathbf{u}_S\mathrm{d}a = 0.
$$

$$\tag{45}$$

Herein, $\bar{q} = n^F\mathbf{w}_F\cdot\mathbf{n}$ is the volume efflux of φ^F over the boundary Γ_q with the outward oriented unit surface normal $\mathbf{n}$ and $\bar{\mathbf{t}} = (\mathbf{T}^S_{E,\text{MECH}} - p\,\mathbf{I})\,\mathbf{n}$ denotes the external load vector

acting on the boundary $\Gamma_{\mathbf{t}}$. Note that the respective *Neumann* boundaries include the surface fractions of all constituents, i.e., solid and fluid, thereby ensuring physically meaningful boundary conditions. However, it is still possible to set conditions for $\bar{q}$ and $\bar{\mathbf{t}}$ at the same surface, while a simultaneous application of a *Dirichlet* and a *Neumann* condition is forbidden according to (44). Following the standard *Bubnov–Galerkin* method, the basis functions for the trial functions of $\mathbf{u}_S$ and $\mathcal{P}$ as well as the corresponding test functions of $\delta\mathbf{u}_S$ and $\delta\mathcal{P}$ are identical. As a result, the respective test functions correspond with the trial functions, which causes $\delta\mathbf{u}_S$ and $\delta\mathcal{P}$ to vanish at *Dirichlet* boundaries $\Gamma_{\mathbf{u}}$ and $\Gamma_{\mathcal{P}}$, where discrete values are prescribed.

As a next step, the weak forms (45) have to be discretised in space, i.e., an appropriate approximation for the unknowns $\mathbf{u}_S$ and $\mathcal{P}$ has to be defined. Concerning the spatial discretisation, i.e., the semi-discretisation with respect to the space variable $\mathbf{x}$, special care must be taken, as the governing equations represent a strongly coupled solid-fluid model, i.e., the unknown field quantities $\mathbf{u}_S$ and $\mathcal{P}$ appear in both equations of (45) (Zienkiewicz and Taylor 2000). Hence, the unknowns have to be approximated simultaneously yielding a so-called mixed finite element formulation. Regarding the volume balance $(45)_1$ of the overall aggregate, the gradient of the hydraulic pressure field needs to be computed, leading to at least a linear discretisation of $\mathcal{P}$. Moreover, as the solid *Cauchy* extra stress tensor $\mathbf{T}^S_{E,\text{MECH}}$ implicitly depends on the gradient of the discretised displacement field $\mathbf{u}_S$, its approximation needs to be one order higher compared with the approximation used for the hydraulic pressure field $\mathcal{P}$. Then, an equal order approximation of the first term in equation $(45)_2$ is achieved. Thus, according to Sandhu and Wilson (1969) the natural choice yields the usage of so-called *Taylor–Hood* elements having quadratic basis functions for the displacement $\mathbf{u}_S$ and linear basis functions for the hydraulic pressure $\mathcal{P}$.

However, regarding numerical accuracy, stability and numerical costs, the suitable choice of mixed finite element formulations is by no means phenomenological, but rather strictly mathematical. In this regard, the inf–sup condition, often referred to as *Ladyshenskaya–Babuška–Brezzi* (LBB) condition, needs to be fulfilled (Brezzi and Fortin 1991; Braess 1997; Wieners 2003). Following this, the *Taylor–Hood* elements fulfil the LBB condition and are the best possible choice from a stability and accuracy point of view. In regard of the complex geometries frequently involved in computational biomechanics, the quadratic discretisation also leads to a good geometry approximation, even with a small number of elements. However, concerning the general 3-d case, the enormous number of mid nodes in finer meshes causes quite large systems of equations, which often have to be solved in parallel (Wieners et al. 2005; Ehlers et al. 2007). One possibility to overcome this problem is to use the

so-called MINI element of Arnold et al. (1984) which has an enriched linear ansatz for $\mathbf{u}_S$ using a bubble node. This leads to stable results but the obtained solution is not as accurate anymore. Note that a linear–linear approximation of $\mathbf{u}_S$ and $\mathcal{P}$ leads to strange instabilities causing mesh dependent solutions due to the so-called spurious pressure modes (Brezzi and Fortin 1991).

Finally, the weakforms (45) have to be discretised in time using a suitable numerical time integration method. In this regard, finite differences are applied using the implicit *Euler* scheme. More detailed information on how the biphasic model is solved using general *Runge-Kutta* methods can be found in Ellsiepen (1999), Diebels et al. (1999) or in the special case of viscoelastic solid deformations in Markert (2005).

As a next step, a brief introduction into the structure of the resulting system of equations is given. Following the abstract illustration of Ellsiepen (1999), the space-discrete variables at N_u nodes are unified in $\boldsymbol{u}$ and the internal variables at N_q quadrature points can be combined to $\boldsymbol{q}$ yielding

$$\left.\begin{array}{l} \boldsymbol{u} = \left[(\mathbf{u}_S^1, \mathcal{P}^1), \ldots, (\mathbf{u}_S^{N_u}, \mathcal{P}^{N_u}) \right]^T, \\ \boldsymbol{q} = \left[C_{Si(kl)}^1, \ldots, C_{Si(kl)}^{N_q} \right]^T \end{array}\right\} \quad \boldsymbol{y} = (\boldsymbol{u}^T, \boldsymbol{q}^T)^T, \quad (46)$$

where $C_{Si(kl)}$ are the six scalar history variables of the symmetric inelastic deformation tensor $\mathbf{C}_{Si}$. If more than one *Maxwell* element is used, the number of inelastic history deformation tensors is increased proportionally. The vector $\boldsymbol{u}$ includes all the nodal degrees of freedom while $\boldsymbol{q}$ contains all the history variables. Note that for the sake of clarity, the different ansatz functions for the solid displacement (quadratic) and the hydraulic pressure (linear) are not regarded in (46). Using the abbreviation $(\,\cdot\,)' := (\,\cdot\,)'_S$, the entire semi-discrete initial-value problem of first order in time can be condensed to

$$\boldsymbol{F}(t, \boldsymbol{y}, \boldsymbol{y}') = \begin{bmatrix} \boldsymbol{g}(t, \boldsymbol{u}, \boldsymbol{u}', \boldsymbol{q}) \\ \boldsymbol{l}(t, \boldsymbol{q}, \boldsymbol{q}', \boldsymbol{u}) \end{bmatrix} = \begin{bmatrix} \boldsymbol{M}\boldsymbol{u}' + \boldsymbol{k}(\boldsymbol{u}, \boldsymbol{q}) - \boldsymbol{f} \\ \boldsymbol{A}\boldsymbol{q}' - \boldsymbol{r}(\boldsymbol{q}, \boldsymbol{u}) \end{bmatrix} \overset{!}{=} \boldsymbol{0}. \quad (47)$$

Herein, initial conditions can be prescribed by applying $\boldsymbol{y}(t_0) = \boldsymbol{y}_0$ at an initial time $t_0 < t$. Moreover, $\boldsymbol{k}$ represents the generalised stiffness vector containing the non-linear dependencies on $(\boldsymbol{u}, \boldsymbol{q})$, while $\boldsymbol{f}$ denotes the vector of the external forces including the *Neumann* load functionals. The property of material incompressibility leads then to a non-regular generalised mass matrix $\boldsymbol{M}$, which turns the global system $\boldsymbol{g}(t, \boldsymbol{u}, \boldsymbol{u}', \boldsymbol{q})$ into a system of differential algebraic equations (DAE). A possible time integration scheme solving this system is the implicit or backward *Euler* scheme which is also used for the computations in the next section. For more information on the systematic comparison of the available time-integration schemes towards their performance, the reader

is referred to Diebels et al. (1999) and Ellsiepen (1999). As the material behaves partly inelastic, the non-linear system $\boldsymbol{g}$ cannot be solved straight forward using *Newton*'s method. Instead, the local system $\boldsymbol{l}(t, \boldsymbol{q}, \boldsymbol{q}', \boldsymbol{u})$ containing the space-discrete evolution equation (28) has to be solved in each step of the global *Newton* iteration. Comparing the structure of (28) with the general structure of $\boldsymbol{l}$ allows for the identification of the regular matrix $\boldsymbol{A}$ with $\boldsymbol{r}$ denoting the rest of the evolution equation. This local system of ordinary differential equations (ODE) is also best suitably solved using the backward *Euler* scheme in combination with a local *Newton* iteration on element level. For more detailed information on this so-called multilevel-*Newton* method, the reader is referred to the comprehensive work of Ellsiepen and Hartmann (2001) and references therein. In this regard, the convergence of *Newton*'s method strongly depends on the consistent linearisation of the non-linear DAE, which will not be given in this paper due to its rather lengthy form. However, apart from the osmotic and anisotropic contributions to the material tangent, a comprehensive description of the missing linearisation of the remaining major parts can be found in Markert (2005).

During every iteration step of the global *Newton* iteration, a finite element code requires an algorithm computing the solid *Cauchy* extra stress tensor $\mathbf{T}_{E,\,\mathrm{MECH}}^S$ at every integration point of the numerical quadrature. According to the known procedure from elastoplasticity, every time the stress needs to be computed in the global iteration, the local ODE have to be solved on element level in order to accumulate the viscoelastic overstress with the isotropic and anisotropic equilibrium parts. The only difference is that no yield criterion has to be checked in the case of viscoelastic material behaviour. As a first step, the actual left solid deformation tensor $(\mathbf{B}_S)^{\mathrm{act}}$ as well as its eigenvalues and eigentensors, needed to compute the purely elastic *Kirchhoff* stress $\boldsymbol{\tau}_{\mathrm{EQ}}^S$, is obtained from the actual solid deformation gradient $(\mathbf{F}_S)^{\mathrm{act}}$. Thereafter, the local *Newton* iteration starts and an independent elastic trial state

$$(\mathbf{B}_{Se})_n^{\mathrm{trial}} = (\mathbf{F}_S)^{\mathrm{act}} (\mathbf{C}_{Si}^{-1})_n^{\mathrm{last}} (\mathbf{F}_S^T)^{\mathrm{act}} \quad (48)$$

is computed via a transport of the last deformation tensor $(\mathbf{C}_{Si}^{-1})_n^{\mathrm{last}}$ taken from the last time step, but using the actual deformation gradient $(\mathbf{F}_S)^{\mathrm{act}}$ as transporting quantity. Once more, the elastic eigenvalues and tensors are calculated, but now in order to obtain the trial overstress $(\boldsymbol{\tau}_{\mathrm{NEQ}}^S)^{\mathrm{trial}}$ from the elastic part of the trial deformation tensor $(\mathbf{B}_{Se})_n^{\mathrm{trial}}$. As the right-hand side of the viscoelastic evolution equation contains the non-equilibrium trial stress expressed in the referential frame, the non-equilibrium trial stress is pulled back using the transport $(\mathbf{S}_{\mathrm{NEQ}}^S)^{\mathrm{trial}} = (\mathbf{F}_S^{-1})^{\mathrm{act}} (\boldsymbol{\tau}_{\mathrm{NEQ}}^S)^{\mathrm{trial}} (\mathbf{F}_S^{T-1})^{\mathrm{act}}$. If the evolution equation is fulfilled on a satisfactory level, the local iteration is stopped and the isotropic *Kirchhoff* stress is finally obtained with the last trial stress satisfying (28).
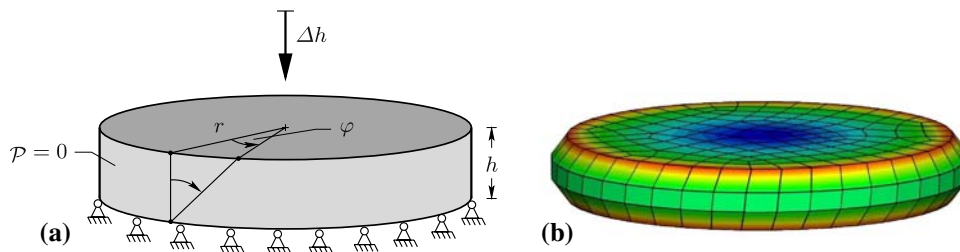
Fig. 3 **a** Average dimensions (radius $r = 4$ mm, height $h = 1.44$ mm) of the cylindrical NP specimen, boundary conditions (vertical displacement $\Delta h = 0.144$ mm, rotation angle φ) and **b** spatial discretisation (441 elements) for the torsion experiment. The *colouring* indicates the qualitative distribution of the shear stress τ after the vertical displacement Δh and the rotation angle φ was applied. Note that the angular outer shape of the deformed specimen in (**b**) is due to the incapability of the post-processing to resolve quadratic elements

The anisotropic contribution is computed thereafter using Eqs. (32) and (42). Together with Eq. (24)$_2$, the sum of the isotropic and anisotropic parts finally yields the purely mechanical solid *Cauchy* extra stress tensor $\mathbf{T}_{E, \text{MECH}}^S$.

Due to the choice of $\mathcal{P}$ as primary variable, the model does not a priori exhibit a stress-free reference configuration. This becomes clear when the overall stress (14) of the model is computed, thereby using values of the natural state, i.e., $\mathbf{u}_S = \mathbf{0}$ and $\mathcal{P} = 0$. Due to (34), there is always an initial osmotic pressure

$$\Delta \pi_{0S} = R\Theta \left[\sqrt{4\, \bar{c}_m^2 + (c_{0S}^{fc})^2} - 2\, \bar{c}_m \right]. \tag{49}$$

Hence, the constant part $\Delta \pi_{0S}\, \mathbf{I}$ is added onto the mechanical extra stress (15) to enforce a stress-free reference configuration in the sense of classical continuum mechanics. Note that without this modification, the model would describe an initial swelling of the tissue until equilibrium between (49) and the tension in the mechanical extra stress (15) is reached. For the sake of this contribution, the described simpler approach is followed and all computations start from a stress free reference configuration having the initial osmotic pressure (49) added onto the mechanical solid extra stress.

6 Numerical examples

6.1 Torsion experiment on a cylindrical NP specimen

The first example addresses the intrinsic viscoelastic material behaviour of the nucleus pulposus in shear. In this context, a numerical torsion experiment is computed, following the real experiments on non-degenerated cylindrical NP specimens performed by Iatridis et al. (1997). Herein, the specimens were harvested from shock frozen IVDs (region L2–L5) and directly placed in a humidity chamber of a testing apparatus. Note that according to the preliminary swelling tests performed by Iatridis et al. (1997), the humidity chamber provides the most stable hydration environment yielding a relatively constant water content of the discs over the three hours of testing time, i.e., no swelling occurs due to the extraction of the specimen from its natural environment. The specimen was then imposed to an axial compression of 10 % of the original height of the disc in order to ensure a sufficient grip between the specimen and the two fully planar and impermeable testing plates, when the angular displacement φ is applied, thereafter. The relaxation of the recorded torque M_T of the top platen was then measured over time, whereas the respective average maximum shear stress τ was computed using the *Saint-Venant* theory for a circular cross section, i.e.,

$$\tau = 2\, M_T / \pi\, r^3, \tag{50}$$

where r is the radius of the cylinder. For the numerical parameter fit of the presented model to the experiments performed in Iatridis et al. (1997), the disc was discretised using 20-noded mixed *Taylor–Hood* elements, as it is seen in Fig. 3.

The upper and lower surface of the disc have movements prevented in the horizontal direction, whereas the upper surface is displacement-driven in axial direction for 0.144 mm and a duration of 2.0 s. This vertical displacement is then held constant over the rest of the computation as well as the hydrostatic pressure $\mathcal{P} = 0$ MPa at the hoop surface and the concentration $\bar{c}_m = 0$ mol/l of the external solution. Six hundred seconds after the vertical displacement was applied, a rotation angle φ is induced within 0.025 s on the top surface and is again held constant for another 600 s, while the relaxation of the torsional shear stress is computed. For a better comparability of the experiments in Iatridis et al. (1997) and in order to overcome the problem of local solution deficiencies, the torque M_T is computed, i.e., the corresponding shear stresses are integrated over the top surface, and afterwards inserted into (50).

In a first approach, the isotropic NP specimen was modelled using one of the simpler material laws included in (39), i.e., the neo-*Hooke* model. In contrast, a total number of two *Maxwell* elements was needed, in order to reproduce the rapid relaxation of the shear stress depicted in Fig. 4.
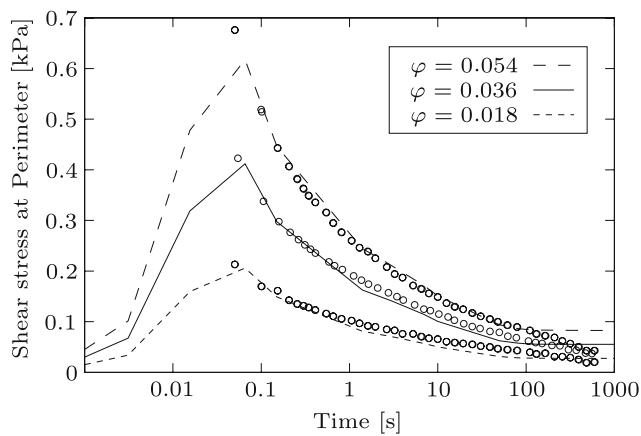
Fig. 4 Results of the parameter fit for the torsion experiment in Iatridis et al. (1997). The lines (*dashed, solid, dotted*) show the shear-stress relaxation of the numerical simulation, while the *dots* are the measured points at three different rotation angles, respectively. The parameter fit was carried out for $\varphi = 0.036$ and held constant for $\varphi = 0.018$ and $\varphi = 0.054$

Herein, the lines indicate the computed curves using the model described above, whereas the circles display the measured values from Iatridis et al. (1997). In this context, the parameters were fit manually to the curve corresponding to an angular displacement of $\varphi = 0.036$. The other two curves, i.e., $\varphi = 0.018$ and $\varphi = 0.054$, were then computed with the identified parameters yielding a good agreement with the measured points.

Some of the respective material parameters for the NP (i.e., μ_j^S, Λ_j^S, η_j^S, and ζ_j^S for $j = 0, 1, 2$) have been fitted using the shear stress-relaxation experiment and are listed in Table 1. As the parameters occurring in (41) have an

influence on the volumetric deformations solely, they can hence not be determined clearly. In this context, the assumption of a constant *Poisson* ratio was made and the relation stemming from the linear theory $\Lambda_j^S = 2\,\mu_j^S\,\nu/(1 - 2\,\nu)$ with $\nu = 0.2$ has been used, even though it is in the strict sense only valid around the natural state. Moreover, it was assumed that the volumetric viscosities have the same values as the solid shear viscosities, i.e., $\zeta_j^S = \eta_j^S$. The parameters γ_j^S were chosen to limit the disc bulge in the swelling experiment of the IVD, as seen in Fig. 5, whereas remaining isotropic parameters (also for the AF as well as for the vertebrae) were taken in accordance to the average values given in Argoubi and Shirazi-Adl (1996), Eberlein et al. (2001), Iatridis et al. (1996, 1997), Lee et al. (2000), Lim and Hong (2000), Ochia and Ching (2002), Shirazi-Adl et al. (1986b), Wu and Chen (1996) and references therein. The parameters for the anisotropic stress contribution (42) were fitted to the regional curves given in Holzapfel et al. (2005). Note in passing that according to Gu et al. (1999) the young AF has an anisotropic permeability which becomes isotropic with age or degeneration. Due to the almost impermeable character of the AF and the fact that the directional variation of the permeability is 'only' of factor two while the values given in literature span over decades, the anisotropic permeability of the AF is neglected in this contribution.

6.2 Swelling experiment of a sagittally cut NP

The second example is concerned with the swelling capability of the presented model. In this context, a swelling

Table 1 Material parameters of the biphasic model for the vertebrae, nucleus pulposus and anulus fibrosus, respectively

Vertebrae: treated with no distinction between cortical shell and spongiosa			
$K_{0S}^S = 2.7 \times 10^{-5}$ (mm²)	$n_{0S}^S = 0.2$ (–)	$\mu_0^S = 192.0$ (MPa)	$\kappa = 0.0$ (–)
$\mu^{FR} = 3.8 \times 10^{-8}$ (MPa·s)	$c_{0S}^{fc} = 0.0$ (mol/l)	$\Lambda_0^S = 88.7$ (MPa)	$\gamma_0^S = 1.0$ (–)
Nucleus pulposus: treated as isotropic, viscoelastic and charged material			
$K_{0S}^S = 3.5 \times 10^{-12}$ (mm²)	$n_{0S}^S = 0.2$ (–)	$\mu_0^S = 0.5$ (kPa)	$\kappa = 0.0$ (–)
$\mu^{FR} = 6.9 \times 10^{-10}$ (MPa·s)	$c_{0S}^{fc} = 0.3$ (mol/l)	$\Lambda_0^S = 0.3$ (kPa)	$\gamma_0^S = 50.0$ (–)
First *Maxwell* element	$\zeta_1^S = 0.37$ (kPa·s)	$\mu_1^S = 2.8$ (kPa)	
	$\eta_1^S = 0.37$ (kPa·s)	$\Lambda_1^S = 1.9$ (kPa)	$\gamma_1^S = 12.0$ (–)
Second *Maxwell* element	$\zeta_2^S = 10.0$ (kPa·s)	$\mu_2^S = 0.85$ (kPa)	
	$\eta_2^S = 10.0$ (kPa·s)	$\Lambda_2^S = 0.57$ (kPa)	$\gamma_2^S = 12.0$ (–)
Anulus fibrosus: treated as inhomogeneous anisotropic charged material			
$K_{0S}^S = 6.2 \times 10^{-12}$ (mm²)	$n_{0S}^S = 0.3$ (–)	$\mu_0^S = 0.95$ (MPa)	$\kappa = 0.0$ (–)
$\mu^{FR} = 6.9 \times 10^{-10}$ (MPa·s)	$c_{0S}^{fc} = 0.1$ (mol/l)	$\Lambda_0^S = 2.2$ (MPa)	$\gamma_0^S = 1.0$ (–)

	Ventro-Lat. Int.	Ventro-Lat. Ext.	Dorsal Int.	Dorsal Ext.
$\tilde{\mu}_1^S$ (kPa)	34.3	146.3	5.9	50.8
$\tilde{\gamma}_1^S$ (–)	44.1	97.1	30.5	54.2

Isotropic contributions are always using the neo-*Hooke*an model and inhomogeneities are modelled as is described in Ehlers et al. (2006a)
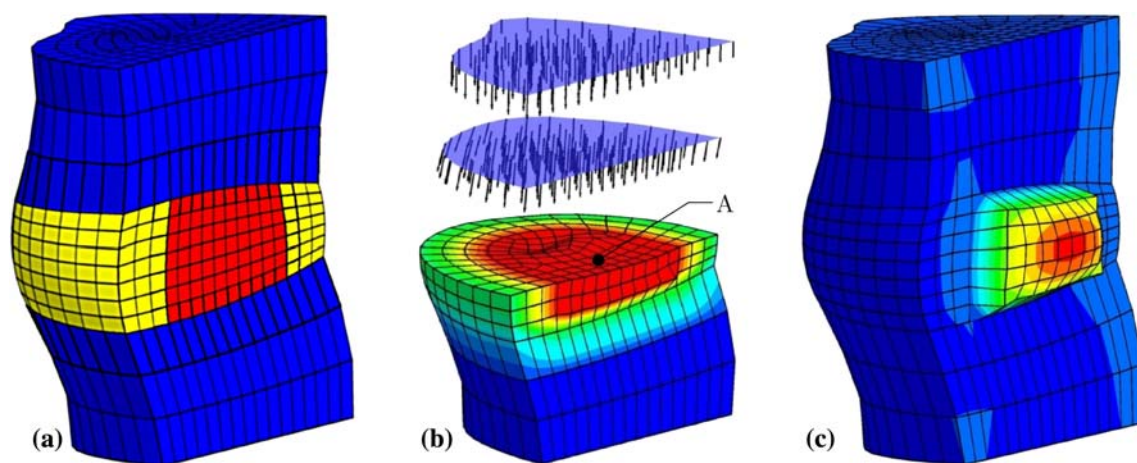
Fig. 5 a Discretisation of the L4-L5 motion segment using 1898 *Taylor–Hood* elements, where the vertebrae are displayed in *blue*, the NP in *red* and the AF in *yellow*. **b** Visualisation at $t = 50$ s, where the *arrows* indicate the seepage velocity of the fluid inside the vertebra and the colours display the osmotic pressure contribution ($red \cong 0.78$ MPa and *blue* 0.0 MPa). **c** The colouring indicates the bulge of the NP with a peak value of 5.7 mm

phenomenon is computed, which occurred while Holzapfel et al. (2005) performed an experiment on a sagittally cut motion segment. Right after the specimen was cut in half and placed on the laboratory table, the NP started to swell out of the IVD and reached a maximum bulge of 4.9 mm, cf. Fig. 4 in Holzapfel et al. (2005).

This behaviour is clearly a result of the tissue being removed from its physiological setting, i.e., the state where the net movement of fluid over the tissue boundary is balanced out between the osmotically driven influx of fluid and the mechanically driven efflux due to the pre-stressed solid skeleton. Whenever this equilibrium is disturbed, the tissue tends to gain chemical equilibrium again. For example, the excess of ions inside the tissue attracts the surrounding fluid with a lower ion concentration to get sucked inside, until equilibrium is reached with the resulting excess of tension in the solid skeleton. The cylindrical NP specimens could not swell as they were not surrounded by any fluid. Even though the sagittally cut motion segment is also not surrounded by a fluid, the IVD is still connected with the adjacent vertebrae, and hence, to the bone marrow. The results of the computation in Fig. 5b shows clearly that the influx of fluid, which is responsible for the bulge, stems from the vertebrae.

The simulations are carried out on a sagittally cut geometry of an L4-L5 motion segment, which is discretised using 1898 20-noded *Taylor–Hood* elements, cf. Fig. 5a, where the vertebrae, the NP, and the AF are highlighted in blue, red and yellow, respectively. The corresponding material parameters are listed in Table 1, whereas the inhomogeneities are modelled as is described in Ehlers et al. (2006a). Following the swelling experiment, only essential boundary conditions

are applied, which do not lead to a mechanical loading of the tissue. In this regard, the top and bottom surfaces of the vertebrae are fixed in space and a drainage ($\mathcal{P} = 0$ MPa) is ensured on all free surfaces. Furthermore, the concentration of the external solution is lowered from $\bar{c}_m = 0.15$ to 0.0 mol/l within 50 s and is then held constantly at zero for another 5000 s.

Figure 5b shows the tendency of the fluid movement when $\bar{c}_m$ reaches zero, i.e., at $t = 50$ s. The seepage velocity of the bone marrow is directed towards the IVD with its maximum osmotic pressure difference $\Delta\pi = 0.78$ MPa indicated in red. The reason for the fluid being attracted by an excess of pressure becomes clear when Fig. 6a is observed, which shows the evolution of p, $\Delta\pi$, and $\mathcal{P}$ measured at point A depicted in Fig. 5b. In the beginning of the computation, i.e., at $t_0 = 0$ s, there is an initial osmotic pressure of $\Delta\pi_0 = 0.31$ MPa, which is solely carried via an 'ingrown' pre-stress in the solid skeleton. Hence, the hydraulic pressure vanishes at $t_0 = 0$ s. As the concentration $\bar{c}_m$ of the surrounding fluid is lowered, the osmotic pressure difference $\Delta\pi$ rises gradually inside the NP and the fluid starts to flow into the IVD to equal out the excess of ions, thereby causing a volume dilatation. However, due to the almost impermeable characteristics of the IVD, the inflow is constrained, and hence, the volume dilatation inside the IVD happens really slowly. Thus, the excess osmotic pressure difference is firstly carried via a suction power of the hydraulic pressure $\mathcal{P}$ (part I in Fig. 6a) and is then gradually released into tension carried by the dilated solid skeleton (part II). The duration of this process is strongly dependent upon the filter velocity of the fluid that gets sucked inside, which is finally a function of the gradient of the negative hydraulic pressure and the
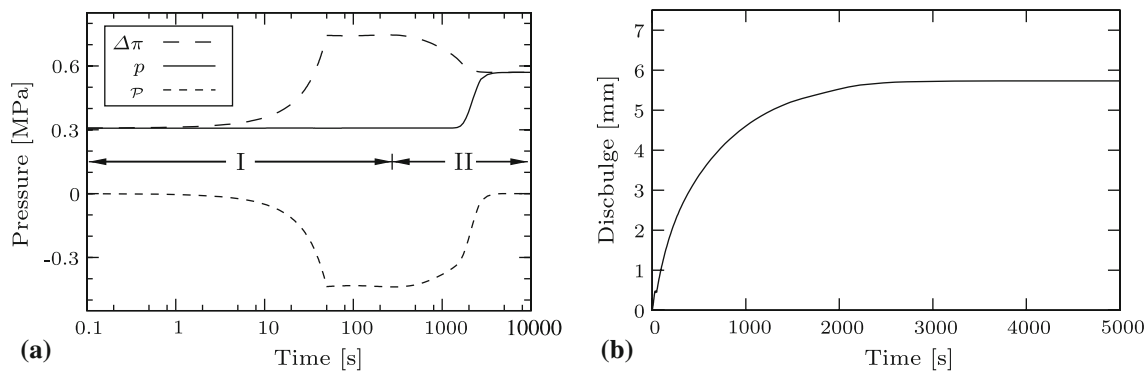
Fig. 6 **a** Evolution of the osmotic pressure difference $\Delta\pi$, the hydraulic pressure $\mathcal{P}$ and the overall pressure p measured at point A, cf. Fig. 5b, inside the NP and **b** development of the NP bulge for the viscoelastic computation of the swelling experiment

resistance (i.e., permeability) of the tissue. In principle, this behaviour is just like a reverse consolidation problem from geomechanics, where a load on the top surface is firstly carried by the pore fluid alone and later via the extra stress of the solid skeleton. Note that if the medium was permeable without any resistance, the consolidation or the swelling process would be finished just after applying the load or concentration drop.

The endpoint of the swelling process is reached, when the negative hydraulic pressure inside the tissue is discharged. According to Fig. 6, this is the case at about $t \approx 3000$ s. The resulting bulge of the NP can be seen in Fig. 5c with the maximum bulge of 5.7 mm, whereas the development of the bulge is depicted in Fig. 6b.

7 Conclusions

Even though the presented numerical examples included only the simpler possibilities of the constitutive equations (39) and (42), the results clearly reveal the high capacity of the model. In this regard, it was the idea to develop a model which includes several levels of complexity, thereby having the advantage of relatively easy identified material parameters on the one hand and the possibility to describe arbitrary material behaviour on the other.

In particular, it is a huge benefit to have a model, which is capable to describe finite deformations with finite material behaviour in the framework of a thermodynamically consistent biphasic theory. In this context, the constitutive equations involved fully satisfy the premise of polyconvexity and therefore, solutions of the numerical approximation are guaranteed. Moreover, it is possible to numerically reproduce all the key functions that occur in charged tissues. On that account any complexity level concerning the mechanical behaviour of the solid skeleton, i.e., viscoelasticity, elasticity and anisotropy, is possible. Regarding the electro-chemical couplings, it is unfortunately not practicable to simultane-

ously have a tri- or quadriphasic model in combination with the presented extended biphasic model, as the resulting set of governing equations cannot be treated in a nice modular manner. Keeping in mind that the model is to be used on complex geometries in combination with other materials in the framework of real applications, the choice was made in favor of the simpler approach to only capture the basic osmotic effects. This is adequate for most of the applications, thereby ensuring a reasonable computation time on today's personal computers.

As a matter of fact, the application range of the model is rather vast. For instance, it is possible to model any soft biological tissue, i.e., cartilage, IVD or brain tissue, as well as hard tissues like bones. Even man-made materials like charged hydro-gel or super-absorbent polymers (SAP), which are able to absorb as much as a thousandfold of their own dry weight, are easily modelled.

The next step in the enhancement of this model is to include degeneration effects like the loss of the fixed charge density which, as a consequence, is often accompanied by calcification, fracture or other mechanical damage. As already seen in the numerical examples, the concentration of the fixed negative charges attracts a certain amount of water, thereby causing a certain extra pressure in the tissue. If this mechanism is disturbed, the basic load-bearing behaviour is modified, and in the case of the IVD, the collagen fibres might be loaded with pressure instead of tension. This again might trigger a cell metamorphosis leading to substantial structural and, therefore, mechanical changes in the tissue. In this context, it is necessary to derive appropriate evolution equations, which trigger the respective damage due to certain mechanical or chemical influences. With focus on the IVD, it is then possible to identify possible mechanisms leading to herniation or calcification of the disc.

References

Argoubi M, Shirazi-Adl A (1996) Poroelastic creep response analysis of a lumbar motion segment in compression. J Biomech 29: 1331–1339

Arnold DN, Brezzi F, Fortin M (1984) A stable finite element for the stokes equations. Calcolo 21:337–344

Ayad S, Weiss JB (1987) Biochemistry of the intervertebral disc. In: Jayson MIV (ed) The lumbar spine and back pain, 3rd edn. Churchill Livingstone, New York pp 100–137

Ayotte DC, Ito K, Perren SM, Tepic S (2000) Direction-dependent constriction flow in a poroelastic solid: The intervertebral disc valve. ASME J Biomech Eng 122:587–593

Bachrach NM, Mow VC, Guilak F (1998) Incompressibility of the solid matrix of articular cartilage under high hydrostatic pressures. J Biomech 31:445–451

Balzani D, Neff P, Schröder J, Holzapfel G (2005) A polyconvex framework for soft biological tissues. Adjustment to experimental data. Int J Solids Struct 43:6052–6070

Biot MA (1941) General theory of three dimensional consolidation. J Appl Phys 12:155–164

Bishop AW (1959) The effective stress principle. Teknisk Ukeblad 39:859–863

Boehler JP (1987) Introduction of the invariant formulation of anisotropic constitutive equations. In: Boehler JP (ed) Applications of tensor functions in solid mechanics, CISM courses and lectures No. 292. Springer, Wien pp 13–30

de Boer R (2000) Theory of Porous Media. Springer, Berlin

Bowen RM (1976) Theory of mixtures. In: Eringen AC (ed) Continuum physics, vol III. Academic Press, New York pp 1–127

Bowen RM (1980) Incompressible porous media models by use of the theory of mixtures. Int J Eng Sci 18:1129–1148

Braess D (1997) Finite elemente. Springer, Berlin

Brezzi F, Fortin M (1991) Mixed and hybrid finite element methods. Springer, New York

Diebels S, Ellsiepen P, Ehlers W (1999) Error-controlled Runge-Kutta time integration of a viscoplastic hybrid two-phase model. Technische Mechanik 19:19–27

Donnan FG (1911) Theorie der Membrangleichgewichte und Membranpotentiale bei Vorhandensein von nicht dialysierenden Elektrolyten. Ein Beitrag zur physikalisch-chemischen Physiologie. Zeitschrift für Elektrochemie und angewandte physikalische Chemie 17:572–581

Ebara S, Iatridis JC, Setton LA, Foster RJ, Mow VC, Weidenbaum M (1996) Tensile properties of nondegenerate human lumbar anulus fibrosus. Spine 21:452–461

Eberlein R, Holzapfel GA, Schulze-Bauer CAJ (2001) An anisotropic model for annulus tissue and enhanced finite element analysis of intact lumbar disc bodies. Comput Methods Biomech Biomed Eng 4:209–229

Eberlein R, Holzapfel GA, Fröhlich M (2004) Multi-segment FEA of the human lumbar spine including the heterogeneity of the anulus fibrosus. Comput Mech 34:147–165

Ehlers W (1989) Poröse Medien–ein kontinuumsmechanisches Modell auf der Basis der Mischungstheorie. Habilitation, Forschungsberichte aus dem Fachbereich Bauwesen, Heft 47, Universität-GH-Essen

Ehlers W (1991) Toward finite theories of liquid-saturated elasto-plastic Porous Media. Int J Plast 7:433–475

Ehlers W (1993) Constitutive equations for granular materials in geomechanical context. In: Hutter K (ed) Continuum mechanics in environmental sciences and geophysics, CISM courses and lectures No. 337. Springer, Wien, pp 313–402

Ehlers W (2002) Foundations of multiphasic and porous materials. In: Ehlers W, Bluhm J (eds) Porous media: theory, experiments and numerical applications. Springer, Berlin, pp 3–86

Ehlers W, Acartürk A (2007) The role of weakly imposed Dirichlet boundary conditions for numerically stable computations of swelling phenomena. Comput Mech (submitted)

Ehlers W, Markert B (2001) A linear viscoelastic biphasic model for soft tissues based on the Theory of Porous Media. ASME J Biomech Eng 123:418–424

Ehlers W, Ellsiepen P, Blome P, Mahnkopf D, Markert B (1999) Theoretische und numerische Studien zur Lösung von Rand-und Anfangswertproblemen in der Theorie Poröser Medien, Abschlußbericht zum DFG-Forschungsvorhaben Eh 107/6-2. Bericht Nr. Nr. 99-II-1 aus dem Institut für Mechanik (Bauwesen), Universität Stuttgart

Ehlers W, Markert B, Acartürk A (2002) Large strain viscoelastic swelling of charged hydrated porous media. In: Auriault JL, Geindreau C, Royer P, Bloch JF, Boutin C, Lewandowska J (eds) Poromechanics II, Proceedings of the 2nd Biot conference on poromechanics, Swets & Zeitlinger, Lisse (Netherlands), pp 185–191

Ehlers W, Markert B, Acartürk A (2005) Swelling phenomena of hydrated porous materials. In: Abousleiman YN, Cheng AHD, Ulm FJ (eds) Poromechanics III, Proceedings of the 3rd Biot Conference on Poromechanics, Balkema Publishers, pp 781–786

Ehlers W, Karajan N, Markert B (2006a) A porous media model describing the inhomogeneous behaviour of the human intervertebral disc. Mater Sci Eng Technol 37:546–551

Ehlers W, Markert B, Karajan N (2006b) A coupled FE analysis of the intervertebral disc based on a multiphasic TPM formulation. In: Holzapfel GA, Ogden RW (eds) Mechanics of Biological Tissue, Springer, Berlin, pp 373–386

Ehlers W, Karajan N, Wieners C (2007) Parallel 3-d simulations of a biphasic porous media model in spine mechanics. In: Ehlers W, Karajan N (eds) Proceedings of the 2nd GAMM Seminar on Continuum Biomechanics, Report No. II-16 of the Institute of Applied Mechanics (CE), Universität Stuttgart, Germany, pp 11–20

Eipper G (1998) Theorie und Numerik finiter elastischer Deformationen in fluidgesättigten Porösen Medien. Dissertation, Bericht Nr. II-1 aus dem Institut für Mechanik (Bauwesen), Universität Stuttgart

Elliott DA, Setton LA (2000) A linear material model for fiber-induced anisotropy of the anulus fibrosus. ASME J Biomech Eng 122: 173–179

Ellsiepen P (1999) Zeit- und ortsadaptive Verfahren angewandt auf Mehrphasenprobleme pröser Medien. Dissertation, Bericht Nr. II-3 aus dem Institut für Mechanik (Bauwesen), Universität Stuttgart

Ellsiepen P, Hartmann S (2001) Remarks on the interpretation of current non-linear finite element analyses as differential–algebraic equations. Int J Numer Methods Eng 51:679–707

Frijns AJH, Huyghe JM, Janssen JD (1997) A validation of the quadriphasic mixture theory for intervertebral disc tissue. Int J Eng Sci 35:1419–1429

Frijns AJH, Huyghe JM, Kaasschieter EF, Wijlaars MW (2003) Numerical simulation of deformations and electrical potentials in a cartilage substitute. Biorheology 40:123–131

Gu WY, Mao XG, Foster RJ, Weidenbaum M, Mow VC, Rawlins B (1999) The anisotropic hydraulic permeability of human lumbar anulus fibrosus. Spine 24:2449–2455

Hassanizadeh SM, Gray WG (1987) High velocity flow in porous media. Transp Porous Media 2:521–531

Hayes WC, Bodine AJ (1978) Flow-independent viscoelastic properties of articular cartilage matrix. J Biomech 11:407–419

Holm S, Nachemson A (1983) Variations in the nutrition of the canine intervertebral disc induced by motion. Spine 8:866–974

Holzapfel GA, Gasser TC (2001) A viscoelastic model for fiber-reinforced composites at finite strains: Continuum basis, computational aspects and applications. Comput Methods Appl Mech Eng 190:4379–4403

Holzapfel GA, Gasser TC, Ogden RW (2004) Comparison of a multilayer structural model for arterial walls with a Fung-type model, and issues of material stability. ASME J Biomech Eng 126:264–275

Holzapfel GA, Schulze-Bauer CAJ, Feigl G, Regitnig P (2005) Monolamellar mechanics of the human lumbar anulus fibrosus. Biomech Model Mechanobiol 3:125–140

Hsieh AH, Wagner DR, Cheng LY, Lotz JC (2005) Dependence of mechanical behavior of the murine tail disc on regional material properties: A parametric finite element study. J Biomech Eng 127:1158–1167

Huyghe JM, Houben GB, Drost MR (2003) An ionised/non-ionised dual porosity model of intervertebral disc tissue. Biomech Model Mechanobiol 2:3–19

Iatridis JC, Weidenbaum M, Setton LA, Mow VC (1996) Is the nucleus pulposus a solid or a fluid? Mechanical behaviors of the human intervertebral disc. Spine 21:1174–1184

Iatridis JC, Setton LA, Weidenbaum M, Mow VC (1997) The viscoelastic behavior of the non-degenerate human lumbar nucleus pulposus in shear. J Biomech 30:1005–1013

Iatridis JC, Setton LA, Foster RJ, Rawlins BA, Weidenbaum M, Mow VC (1998) Degeneration affects the anisotropic and nonlinear behaviors of human anulus fibrosus in compression. J Biomech 31:535–544

Iatridis JC, Laible JP, Krag MH (2003) Influence of fixed charge density magnitude and distribution on the intervertebral disc: Applications of a Poroelastic and Chemical Electric (PEACE) model. Trans ASME 125:12–24

Kaasschieter EF, Frijns AJH, Huyghe JM (2003) Mixed finite element modelling of cartilaginous tissues. Math Comput Simul 61:549–560

Kleiber M (1975) Kinematics of deformation processes in materials subjected to finite elastic–plastic strains. Int J Eng Sci 13:513–525

Klisch SM, Lotz JC (1999) Application of a fiber-reinforced continuum theory to multiple deformations of the annulus fibrosus. J Biomech 32:1027–1036

Klisch SM, Lotz JC (2000) A special theory of biphasic mixtures and experimental results for human annulus fibrosus tested in confined compression. ASME J Biomech Eng 122:180–188

Lai WM, Hou JS, Mow VC (1991) A triphasic theory for the swelling and deformation behaviors of articular cartilage. ASME J Biomech Eng 113:245–258

Laible JP, Pflaster DS, Krag MH, Simon BR, Haugh LD (1993) A poroelastic-swelling finite element model with application to the intervertebral disc. Spine 18:659–670

Lanir Y (1987) Biorheology and fluid flux in swelling tissues. I. Bicomponent theory for small deformations, including concentration effects. Biorheology 24:173–187

Lee CK, Kim YE, Lee CS, Hong YM, Jung JM, Goel VK (2000) Impact response of the intervertebral disc in a Finite-Element Model. Spine 25:2431–2439

Lee EH (1969) Elastic–plastic deformation at finite strains. J Appl Mech 36:1–6

Li LP, Soulhat J, Buschmann MD, Shirazi-Adl A (1999) Nonlinear analysis of cartilage in unconfined ramp compression using a fibril reinforced poroelastic model. Clin Biomech 14:673–682

Li LP, Shirazi-Adl A, Buschmann MD (2003) Investigation of mechanical behavior of articular cartilage by fibril reinforced poroelastic models. Biorheology 40:227–233

Lim TH, Hong JH (2000) Poroelastic properties of bovine vertebral trabecular bone. J Orthop Res 18:671–677

Marchand F, Ahmed AM (1990) Investigation of the laminate structure of the lumbar disc anulus. Spine 15:402–410

Markert B (2005) Porous media viscoelasticity with application to polymeric foams. Dissertation, Bericht Nr. II-12 aus dem Institut für Mechanik (Bauwesen), Universität Stuttgart

Markert B (2007) A constitutive approach to 3-d nonlinear fluid flow through finite deformable porous continua with application to a high-porosity polyurethane foam. Transp Porous Media 70:427–450

Markert B, Ehlers W, Karajan N (2005) A general polyconvex strain-energy function for fiber-reinforced materials. Proc Appl Math Mech 5:245–246

Mooney M (1940) A theory of large elastic deformation. J Appl Phys 11:582–592

Mow VC, Hayes WC (1997) Basic orthopaedic biomechanics. Lippincott-Raven, New York

Mow VC, Kuei SC, Lai WM, Armstrong CG (1980) Biphasic creep and stress relaxation of articular cartilage in compression: theory and experiments. ASME J Biomech Eng 102:73–84

Mow VC, Gibbs MC, Lai WM, Zhu WB, Athanasiou KA (1989) Biphasic indentation of articular cartilage. II. A numerical algorithm and an experimental study. J Biomech 22:853–861

Noll W (1958) A mathematical theory of the mechanical behavior of continous media. Arch Rat Mech Anal 2:197–226

Ochia RS, Ching RP (2002) Hydraulic resistance and permeability in human lumbar vertebral bodies. J Biomech Eng 124:533–537

Parent-Thirion A, Macías EF, Hurley J, Vermeylen G (2007) Fourth European Working Conditions Survey. European Foundation for the Improvement of Living and Working Conditions, Dublin

Raspe H, Hueppe A, Neuhauser H (2008) Back pain, a communicable disease?. Int J Epidemiol 37:69–74

Reese S, Govindjee S (1998) A theory of finite viscoelasticity and numerical aspects. Int J Solids Struct 35:3455–3482

Riches PE, Dhillon N, Lotz J, Woods AW, McNally DS (2002) The internal mechanics of the intervertebral disc under cyclic loading. J Biomech 35:1263–1271

Rivlin RS (1948) Large elastic deformations of isotropic materials. Proc R Soc Lond Ser A 241:379–397

Sandhu RS, Wilson EL (1969) Finite-element analysis of seepage in elastic media. ASCE J Eng Mech Div 95:641–652

Schanz M, Diebels S (2003) A comperative study of biot's theory and the linear Theory of Porous Media for wave propagation problems. Acta Mech 161:213–235

Schmidt CO, Raspe H, Pfingsten M, Hasenbring M, Basler HD, Eich W, Kohlmann T (2007) Back pain in the german adult population. Prevalence, severity, and sociodemographic correlations in a multiregional survey. Spine 32:2005–2011

Schröder J, Neff P (2003) Invariant formulation of hyperelastic transverse isotropy based on polyconvex free energy functions. Int J Solids Struct 40:401–445

Schröder Y, Sivan S, Wilson W, Merkher Y, Huyghe JM, Maroudas A, Baaijens FPT (2007) Are disc pressure, stress and osmolarity affected by intra- and extrafibrillar fluid exchange. J Orthop Res 25:1317–1324

Shirazi-Adl A (1994) Nonlinear stress analysis of the whole lumbar spine in torsion-mechanics of facet articulation. J Biomech 27:289–299

Shirazi-Adl A (2006) Analysis of large compression loads on lumbar spine in felxion and torsion using a novel wrapping element. J Biomech 39:267–275

Shirazi-Adl A, Ahmed AM, Shrivastava SC (1986a) A finite element study of a lumbar motion segment subjected to pure sagittal plane moments. J Biomech 19:331–350

Shirazi-Adl A, Ahmed AM, Shrivastava SC (1986) Mechanical response of a lumbar motion segment in axial torque alone and combined with compression. Spine 11:914–927

Skaggs DL, Weidenbaum M, Iatridis JC, Ratcliffe A, Mow VC (1994) Regional variation in tensile properties and biochemical composition of the human lumbar anulus fibrosus. Spine 19:1310–1319

Skempton AW (1960) Significance of Terzaghi's concept of effective stress (Terzaghi's discovery of effective stress). In: Bjerrum L, Casagrande A, Peck RB, Skempton AW (eds) From theory to practice in soil mechanics. Wiley, New York pp 42–53

Spencer AJM (1972) Deformations of fiber-reinforced materials. Oxford University Press, NY, USA

Spencer AJM (1982) The formulation of constitutive equations for anisotropic solids. In: Boehler JP (ed) Mechanical behavior of anisotropic solids, Proceedings of the Euromech Colloquium, vol 115, Martinus Nijhoff Publishers, The Haque, pp 2–26

Spencer AJM (1984) Constitutive theory for strongly anisotropic solids. In: Spencer AJM (ed) Continuum theory of the mechanics of fibre reinforced composites, CISM Courses and Lectures No. 282. Springer, Wien pp 1–32

Sun DN, Gu WY, Guo XE, Lai WM, Mow VC (1999) A mixed finite element formulation of triphasic mechano-electrochemical theory for charged, hydrated biological soft tissues. Int J Numer Methods Eng 45:1375–1402

Treloar LRG (1975) The physics of rubber elasticity, 3rd edn. Clarendon Press, Oxford

Truesdell C (1949) A new Definition of a Fluid, II. The Maxwellian fluid. Tech. Rep. P-3553, § 19, US Naval Research Laboratory

Urban J, Holm S (1986) Intervertebral disc nutrition as related to spinal movements and fusion. In: Hargens AR (ed) Tissue nutrition and viability. Springer, Berlin, pp 101–119

Urban JPG, Roberts S (1996) Intervertebral disc. In: Comper WD (ed) Extracellular matrix, vol 1, Tissue function. Harwood Academic Publishers GmbH, pp 203–233

van Loon R, Huyghe FM, Wijlaars MW, Baaijens FPT (2003) 3D FE implementation of an incompressible quadriphasic mixture model. Int J Numer Methods Eng 57:1243–1258

Varga OH (1966) Stress–strain behavior of elastic materials. Interscience, New York

Wieners C (2003) Taylor–Hood elements in 3D. In: Wendland WL, Efendiev M (eds) Analysis and simulation of multified problems. Springer, Berlin pp 189–196

Wieners C, Ehlers W, Ammann M, Karajan N, Markert B (2005) Parallel solution methods for porous media models in biomechanics. Proc Appl Math Mech 5:35–38

Wilson W, van Donkelar CC, Huyghe JM (2005) A comparison between mechano-electrochemical and biphasic swelling theories for soft hydrated tissues. ASME J Biomech Eng 127:158–165

Wu JSS, Chen JH (1996) Clarification of the mechanical behavior of spinal motion segments through a three-dimensional poroelastic mixed finite element model. Med Eng Phys 18:215–224

Zienkiewicz OC, Taylor RL (2000) The finite element method: the basis, vol 1, 5th edn. Butterworth Heinemann, Oxford